Tracking pollutants using Lagrangian Coherent Structures.

By

Amengor Cyril Makafui
(10638272)

June 2018

THIS THESIS IS SUBMITTED TO THE UNIVERSITY OF GHANA,
LEGON IN PARTIAL FULFILMENT OF THE REQUIREMENTS
FOR THE AWARD OF MASTER OF PHILOSOPHY
MATHEMATICS DEGREE.

DECLARATION

This thesis was written in the Department of Mathematics, University of Ghana, Legon from August 2017 to July 2018 in partial fulfilment of the requirements for the award of Master of Philosophy degree in Mathematics under the supervision of Dr. Joseph K. Ansong and Dr Anton Asare-Tuah of the University of Ghana.

I hereby declare that except where due acknowledgement is made, this work has never been presented wholly or in part for the award of a degree at the University of Ghana or any other University.

Signature:..
Student: Amengor Cyril Makafui
cyril@aims.edu.gh

Ansong
Signature: ....
Dr. Joseph K. Ansong

Signature: ....
Dr. Anton Asare-Tuah

ABSTRACT

In steady flows, the notion of boundaries separating dynamically distinct regions is not ambiguous. This is because the invariant manifolds of time-independent flows and the critical points of time-periodic flows provide adequate information to determine the behaviour of the solutions of these systems. However, for time dependent systems, it is strenuous to determine the nature of their solutions due to their dependence on time. Nevertheless, it was observed that just like steady flows, most time-dependent systems have boundaries that prevent cross-mixing of dynamically distinct regions. They are known as Lagrangian Coherent Structures(LCSs) and they are embedded in time-dependent flows as robust structures that determine the flow pattern of fluid particles.

This project investigates LCSs and also employs a numerical method to compute the Finite Time Lyapunov Exponent to detect these structures. Initially, the coherent structures are defined as hyperbolic material lines that separate dynamically distinct regions in an unsteady flow. Then, the LCSs are classified into attracting and repelling structures based on their influence on the time-dependent flow. Subsequently, the LCSs are also defined as a second derivative ridges of the FTLE fields. This definition is perceptible from the numerical computations of the double-gyre model where the coherent structures are extracted as ridges of the computed FTLE fields. Furthermore, we employ the Finite time Lyapunov Exponent model to carry out numerical simulations on satellite observed surface velocities along the coast of Ghana. The aim of this realistic application is to determine the Lagrangian Coherent Structures that are formed in geophysical flows. Finally, based on these results, we hypothesize the implications of a crude oil spill along the coast of Ghana. It was realized that in the event of a spill, the oil is likely to be confined to the coast temporarily due to the concentration of repelling LCSs. Also, for a longer time interval the oil spill is likely to be advected from the coastline.

DEDICATION

I dedicate this project work to my family and to the late Prof. Francis K. A Allotey (AIMS Ghana, Founder).

ACKNOWLEDGEMENTS

My greatest thanks is to God Almighty for granting me good health and replenishing my strength daily through the course of this project. Secondly, in line with the famous quote of Sir Isaac Newton which says "If I have seen further it is by standing on the shoulders of Giants", I would express my gratitude to Dr Joseph K. Ansong for allowing me to stand on his shoulders. It has been a great learning experience. Also to Dr. Anton Asare-Tuah, thanks for all the encouraging words.

To Dr. Ralph Twum; Head of Mathematics Department and Lecturers thanks so much for giving me the platform to aspire for academic excellence. Also my sincere gratitude to Mr. Bennett Foli for the help you offered to me in understanding and working on the satellite data. To all my colleagues Some, Hannah and Esther I am very grateful for all your ideas and help you rendered to me throughout the course of this project. Finally not forgetting my God given friend Dzifa, thank you for all your encouraging words and support despite your busy schedule.

Contents

Chapter 1

Introduction

Since time immemorial human beings have devised various techniques for solving complex-life problems, however, in spite of all the technological advancements, one major challenge remaining is the problem of pollution. Pollution is defined as the release of unwanted substances into the natural environment that cause adverse changes. Also [3] describes pollution as the addition of any substance or any form of energy such as radioactivity into the environment at a rate faster than it can be dispersed, diluted, decomposed, recycled or stored in some harmless form. Pollution exist in several forms such as land, water and air just to name a few. In August 2006, toxic waste produced by a Singaporean oil company called Trafigura Beheer BV, was offloaded to an Ivorian waste handling company. The company then discarded the waste at the port of Abidjan. Subsequently, this resulted in the contamination of their water bodies and also caused a lot of infections due to the presence of Hydrogen Sulphide in the waste. The aftermath of this event resulted in 17 deaths and about $100,000$ inhabitant needed critical medical attention [28]. Later on in April 2010, airborne volcanic ash caused pandemonium in European airspaces. This natural disaster led to the grounding of several commercial airlines because the atmosphere was not suitable for air plane operations. These airline companies incurred huge debts. Finally in that same month, the world recorded the greatest oil spill in history. An oil drilling rig in the Gulf of Mexico exploded leading to the enormous spillage of oil on the Pacific Ocean. Consequently it had adverse effects on aquatic life. Numerous aquatic plants and organisms died. According to [4], 78% of the oil spill still remain in the Gulf of Mexico.

Due to these three globally significant events, it was of paramount importance to propose a solution to help control and detect pollutants. Scientists from diverse fields suggested different approaches to help track the movement of these pollutants in fluids. One such method is to run complex three-dimensional ocean models such as the Modular Ocean Model(MOM), the Hybrid Coordinate Ocean Model(HYCOM) or the Massachusetts Institute of Technology General Circulation Model(MITgcm). However, these global and regional ocean models are quite expensive to run numerically. They also require relatively more simulation time before results can be obtained to help alleviate the impact of a disaster. Due to this reason, one of the proposed methods to help track pollutants is to employ dynamical system theory. This theory is a field in mathematics used to describe complex systems, usually by employing differential equations [14]. A dynamical system is defined as a system that describes the time dependence of a point in geometrical space [5]. There are three main groups, namely: the time independent, the time- periodic and the time dependent systems. For time-independent and periodic flows the behaviour of the system can be determined for any given point. The phase portraits of time-independent flows provides additional details about the behaviour of their solutions. There are four main phase portraits generated for these steady flows namely the node, focus, center and the saddle point. The importance of studying these plots is to identify the concept of boundaries in the flow which separate dynamically distinct regions. This is mostly visible in saddle plots where the invariant manifolds act as the boundary within the flow. Furthermore for time-dependent flows, due to their reliance on time, the behaviour of the systems is unpredictable. Nevertheless from numerous research work done on time-dependent flows, it has emerged that there are structures in the flow that act as boundaries thereby shaping the advection of particles. These barriers are known as Lagrangian Coherent Structures (LCSs).

LCSs are time-evolving structures that shape trajectory patterns in complex dynamical systems [21]. The Lagrangian term describes the movement of the particles through fluids. In $2D$ flows, LCSs appear as material lines (continuous, smooth) curves that determine the direction of particles as they are advected in the flow. The LCSs detection methods provide predictive capabilities, by identifying robust structures that are too strong to be destroyed by short-term fluctuations in the flow field. These surfaces are classified into elliptic, parabolic and hyperbolic barriers depending on the type of influence they exhibit on neighbouring fluid particles [8]. However this project focuses on the hyperbolic barriers. These barriers behave as the invariant manifolds of the steady flows by attracting or repelling other material elements in the flow. Some examples of dynamical systems that employ the concept of LCSs are Chlorophyll patterns in the ocean[12], surface drifters[16], clouds of volcanic ash[23], oil spills[17] and spores in the atmosphere[26]. One approach that may be used for detecting these structures in unsteady flows is by running regional ocean models to simulate the advection of tracers in the flow. The regional ocean models are based on the Eulerian approach of viewing the flow field. With this method, it focuses on specific locations or regions in space as time elapses. As mentioned before it is computationally expensive to run regional models, and in addition minor errors with the initial conditions would result in a faulty result.

One of the most important diagnostic techniques for detecting LCSs in unsteady fluid flows is by computing the Finite time Lyapunov Exponent (FTLE). FTLE has proven to be an effective tool in analyzing unsteady flows. Hitherto numerous computational techniques that have been proposed to study LCSs have not been as efficient as the FTLE. The FTLE is a scalar value which determines the amount of stretching about the trajectory point of fluid particles. It can also be defined as a scalar value that determines the separation of minute particles in an unsteady flow over a finite time interval [27]. Additionally, it varies as a function of time and space. Although FTLE's are derived from Eulerian methods, it is considered as Lagrangian because it considers individual fluid particles in the flow. They are able to predict the succeeding positions of fluid particles based on the history of the flow. Therefore, the study of LCSs and FTLE is not just for the sake of academic curiosity but they have yielded ground-breaking results in tracking pollutants[22].

1.1 Research Objectives

The main objectives of this project include understanding the concept of dynamical systems in relation to autonomous, time-periodic and time dependent systems. Our specific objectives are:

1. To carry out a detailed study of LCSs and how they apply to fluid dynamics.
2. To compute the FTLE field in simple fluid systems in order to detect LCSs in steady and unsteady flows.
3. Perform numerical computations of FTLE from satellite observed surface velocity fields along the coast of Ghana.

Section 1.3: Outline

Chapter 1 gives a brief introduction of some key terminologies used in the project. Chapter 2 discusses the findings of some research papers which would be vital for this project. Chapter 3 explores the properties of the dynamical systems in detail, such as the equations governing LCSs and the FTLE. In Chapter 4, we carry out numerical simulations for the FTLE and the last chapter is the conclusion.

Chapter 2

Literature Review

LCSs are defined by [7] as time-evolving material surfaces or lines that shape trajectory patterns in complex dynamical systems such as geophysical flows and multi-body problem such as the movement of celestial objects. Detecting these surfaces in unsteady flows is challenging. Nevertheless, [7] proposed an algorithm that study unsteady velocity data using the variational theory of hyperbolic LCSs in $2D$ flows. Firstly, the paper shows that the LCSs are the most attracting or repelling material lines in a geophysical flow. It considered the advection of a material surface denoted as $M(t)$ within a given time interval. In addition the normal repulsion rate was determined for $M(t)$ along the trajectory patterns. From the outcome, it was observed that when the repulsion rate is greater than 1, then the material line is a repelling LCSs and vice-versa. These coherent structures are collectively called the hyperbolic LCSs. Subsequently, [7] carried out numerical simulations to determine strainlines in flow. Strainlines are defined as curves tangent to the eigenvector field of the Cauchy green deformation tensor. The equation for the deformation tensor is given as

$$C_{t_0}^{t_0+T}(x_0) = \left(\nabla F_{t_0}^{t_0+T}(x_0)\right)^* \nabla F_{t_0}^{t_0+T}(x_0).$$

Where $F_{t_0}^{t_0+T}(x_0)$ represents the flow map from initial position x_0 from initial time t_0 to final time $t_0 + T$ and $\nabla F_{t_0}^{t_0+T}(x_0)$ denotes the Jacobian of the flow map. Additionally, the star represents the matrix transposition. The Cauchy deformation tensor is symmetric and positive definite hence it admits two real positive eigenvalues and orthogonal real eigenvectors [7]. Also the eigenvectors are defined on a subspace called the strain direction. One of the results of [7] is that strainlines are used to locate and advect hyperbolic LCS over a given interval. However, some challenges were faced in the computations of the strainlines namely: sensitivity of strain direction and degenerate points. For the deformation tensor, the eigenvectors are very sensitive to computational errors. These errors are most likely near hyperbolic LCSs due to the large deviations in close particles. This results in huge mistakes in the computation of the Cauchy deformation tensor. Subsequently, degenerate points are produced when the eigenvalues of the deformation tensor are equal. The tensor field then becomes a scalar multiple of the identity matrix therefore the eigenvectors at these points are not well defined [7]. Finally, the algorithm was tested on $2D$ turbulence with the velocity field derived as the numerical result of the Navier-Stokes equation [7]. The main findings of this paper are that LCSs are attracting and repelling material lines and the tangents of $M(t)$ can be employed to determine the advection of LCSs using a higher-order Hermite interpolation.

[11] defined LCSs as regions of qualitatively different tracer dynamics. Tracers are particles embedded in geophysical flows that determine the flow patterns in the fluids. The two main types are active and passive tracers. For the former, they change the flow pattern by transforming the properties of fluids and the latter do not have any effect on the flow. Therefore the latter is essential in determining coherent structures in the flow. [11] investigated the role of the LCSs in the mixing of $2D$ turbulence. Similar to [7] LCSs boundaries are defined as stable and unstable material lines, however, for turbulent flows due to the lack of regular time dependence the material lines are tracked for all given time intervals to determine their stability or instability[11]. Since it's not possible, [11] proposed the finite-time stability and instability method for detecting stable and unstable material lines. This approach is derived from the concept of uniform normal hyperbolicity for dynamical systems. Therefore [11] defined LCSs boundaries as material lines with locally the longest or shortest stability or instability points in turbulent flows. Lastly, an algorithm was developed and tested on a barotropic turbulence and was compared with the Lagrangian Statistics. It was observed that the algorithm was able to detect mesoscale structures whilst the Statistical method was not. Moreover, the algorithm can also be used to isolate votex cores and regions with distinct hyperbolicity levels [11].

[21] described FTLE as a measure of sensitivity of a fluid particle's future behaviour to its initial position in a flow field. Initially, [21] investigated the two main perspectives of fluid flow namely the Eulerian and Lagrangian approaches. The eulerian method looks at the fluid properties at a fixed point in space and time. Conversely, the Lagrangian considers the individual elements of the fluid for varying space and time. Therefore it is able to track changing velocity of individual fluid elements as

they are advected in the flow [21]. This makes the Lagrangian method the best tool for studying material advection in geophysical flows. In understanding how the Lagrangian method is relevant in fluid transport, [21] investigated the double-gyre. The double-gyre is a model that is generated by a set of equations and it consist of two oppositely swirling vortices whose strengths and locations vary with time [21]. In this paper, [21] studied the advection of a circular drop of a dye in a $2D$ time periodic flow in the interval $[t_0, t_1]$. It was observed at t_1 that the dye is stretched and advected throughout the periodic flow. Also, the dye is separated into two distinct regions represented as red and blue curves by a boundary in the flow which is depicted as a white line. This boundary represents the strongest repelling LCSs and it is responsible for the separation of the circular blob of dye. Therefore, the two distinct regions can be considered as representing the crude oil and water. Due to the success of this experiment, the LCS approach was employed to study the satellite data for the oil spill on the deep-water horizon off the Gulf of Mexico. As a result, it was discovered that the attracting LCSs determine the advection of the Oil spill by hindcasting. Hindcasting is a process of predicting a previous event based on the data gathered earlier. Subsequently, [21] realized that future events can be determined based on the current information by forecasting. This method is able to locate major transport barriers in unsteady flows such as eddies and vortices. However, the satellite data must be comprehensive, reliable and up-to-date [21].

Finally, [24] introduced a different but a well founded approach to obtaining LCSs in fluid flows. The paper defined LCSs as ridges of FTLE fields. The ridges are defined as special gradient lines of the field that are transverse in the direction of the minimum curvature [24]. First and foremost, two mathematical definitions were proposed for a LCSs. The first definition considered the LCSs as the curvature ridges of the FTLE field and it was derived from the principal curvature and the direction of material surfaces in differential geometry [18]. Also the LCSs were defined as the second derivative ridge of an FTLE field and it is relies on the Hessian of the FTLE. The Hessian is given as [24]

$$\sum = \frac{d^2\sigma_{t_0}^{T}(x)}{dx^2}.$$

where $\sigma_{t_0}^{T}(x)$ represents the FTLE values at x. In addition, [24] determined the Lagrangian properties of the FTLE. [24] realised that the FTLE values are Lagrangian for large integration times, however, that does not necessarily mean the LCSs obtained from these computations are Lagrangian. This is because the LCSs are obtained from the computations of higher derivatives of the FTLE fields [24]. Lastly, numerical computations were carried out on three examples namely the double gyre model and the Very high frequency(VHF) data along the coast of Florida. In the first example, the paper analyzed the time independent and dependent gyre models. In both models, the low and high FTLE fields act as the attracting and repelling LCSs. Also for the subsequent example the flux across the LCSs was determined to be less than 0.05% [24]. Therefore, fluid particles are not likely to cross the LCSs in the flow. In conclusion, LCSs are ridges in FTLE fields and also LCSs and FTLE provide a more suitable approach in studying transport and mixing in unsteady flows.

Chapter 3

Dynamical Systems

3.1 Introduction

This chapter introduces the basic understanding of the three types of dynamical systems. Their properties would be illustrated by solving simple examples as a prelude to the more complicated concepts of LCSs and FTLE to be discussed later.

Introduction to Dynamical Systems

Dynamical systems are systems in which a function describes the time dependence of a point in a geometrical space. It can also be defined as a model that explains the temporal evolution of a system. These systems are governed by a set of variables known as the state variables. If the values for these variables are known for any given time, then the state of the system can be determined. Therefore, the state variables provide a detailed description of the system at any given point in time. The general form of the dynamical system is expressed as

$$\begin{cases} \mathbf{x}^{'}\left(t; t_0, \mathbf{x}_0\right) = \mathbf{v}\left(\mathbf{x}\left(t; t_0, \mathbf{x}_0\right), t\right) \\ \\ \mathbf{x}\left(t_0; t_0, \mathbf{x}_0\right) = \mathbf{x}_0 \end{cases} \tag{3.1}$$

From equation (3.1), t, t_0, x_0 and x represent the initial time, final time, starting and final positions respectively. In addition, $x(t; t_0, x_0)$ and $\mathbf{v}\left(\mathbf{x}\left(t; t_0, \mathbf{x}_0\right), t\right)$ represent the state variables and the velocity vectors of the dynamical system respectively. Applications of dynamical systems are ubiquitous in our daily activities, some of these include the swinging of a pendulum, the growth of bacteria and the movement of fluids. Based on their dependence on time, these systems are grouped into three main categories, namely Time-independent, Time-periodic and Time-dependent systems.

3.2 Linear and Non-linear systems

The equations of all dynamical systems are classified under these two main categories. They can either be linear or non-linear. Linear systems are systems that follow the principle of superposition. The principle of superposition is defined by the following laws:

i. Law of additivity: Let $f(u_1) = y_1$ and $f(u_2) = y_2$. Therefore, $f(u_1+u_2) = y_1+y_2$.

ii. Law of homogeneity: let $f(u) = y$ and A be a scalar, then $f(Au) = Ay$

For a system to be considered linear, it must satisfy both laws. However, most real life applications of dynamical systems such as the predator-prey model and the Naiver-Stokes equation are defined by non-linear equations. Non-linear systems are systems which do not follow the principle of superposition. With these systems, it is realised that either only one of the laws of superposition is satisfied or none at all. However, there are two main methods employed in solving for non-linear systems namely: the linearisation method and Lyapunov function. The linearisation method involves linearising a non-linear system. The first step includes determining the equilibrium, fixed or critical points of the non-linear system. Secondly, the Jacobian matrix of each fixed point is computed. Finally the eigenvalues and eigenvectors are determined for the equilibrium points. This helps to determine the stability of the system based on the eigenvalues. However, the linearisation method does not work on all non-linear systems. For example, if complex eigenvalues with no real parts are obtained after linearisation, it would be difficult to determine the nature of the non-linear system. Therefore, in such cases the Lyapunov function can be used to determine the stability of the equilibrium point. Lyapunov functions are scalar functions that are used to determine the stability of non-linear differential equations [13]. These functions are based on the following definitions

Consider a non-linear system of the form:

$$\mathbf{x}' = f(x)$$

where the function $f = (f_1, ..., f_n)$ and the partial derivatives are assumed to be continuous in an open set $\mathbb{U} \in \mathbb{R}^n$ consisting of the origin. Let $V(\mathbf{x})$ be a vector continuous function defined in $\mathbb{U}$ and $V(0) = 0$. Then, the following definitions hold

I. $V(\mathbf{x})$ is positive definite in $\mathbb{U}$ if and only if $V(\mathbf{x}) > 0$ for all $x \neq 0$, $\mathbf{x} \in \mathbb{U}$.

II. For $V(\mathbf{x}) \geqslant 0$ in $\mathbb{U}$ for all $\mathbf{x} \in \mathbb{U}$, $V(\mathbf{x})$ is said to be positive semi-definite.

III. For $V(\mathbf{x}) < 0$ in $\mathbb{U}$ for all $\mathbf{x} \in \mathbb{U}$, $V(\mathbf{x})$ is said to be negative definite.

IV. For $V(\mathbf{x}) \leqslant 0$ in $\mathbb{U}$ for all $\mathbf{x} \in \mathbb{U}$, $V(\mathbf{x})$ is said to be negative semi-definite.

These definitions are essential in checking for the stability, asymptotic stability and instability of the trivial solutions or the fixed points of non-linear autonomous systems. In subsequent sections we will consider some examples of both linear and non-linear dynamical systems.

3.3 Phase Portrait of dynamical systems

A phase portrait is defined as a geometrical representation of the solutions of a dynamical system in the phase plane. Where the phase plane simply refers to the Cartesian plane. Also, the phase portrait gives a detailed insight about the general properties of the system by visualizing how the solutions of a system of differential equations would behave with time. The phase plots for linear systems can be determined by the eigenvector method. With this method, the eigenvalues determine the direction of the trajectories that separate the portrait into distinct regions based on the behaviour of the system. These trajectories are known as the separatrices. Also, the critical/equilibrium points of a dynamical system are the points where the system has a constant solution. In sketching the plots of linear systems, the sign of the eigenvalue is critical. Positive eigenvalues generate plots with trajectories that move away from the origin with time. They are known as unstable manifolds. Subsequently negative eigenvalues produce plots with trajectories moving towards the origin with time and they are referred to as stable manifolds.

In the case of non-linear systems, we may have to apply the linearisation theorem and then consider the system as a linear function. Also the Lyapunov function is applied to non-linear systems that cannot be linearised. All computations for most parts of the project are in $\mathbb{R}^2$.

3.3.1 Real and distinct eigenvalues

(i) When the eigenvalues are both positive, that is $(0 \leq \lambda_1 \leq \lambda_2)$, the phase portrait is an unstable node.

(ii) When the eigenvalues are both negative, that is $(\lambda_1 \leq \lambda_2 \leq 0)$, the plot is a stable node.

(iii) When the eigenvalues are positive and negative $\lambda_1 \leq 0 \leq \lambda_2$, the plot is a saddle.

3.3.2 Repeated eigenvalue

(i) When the eigenvalues are positive $(\lambda_1, \lambda_2 \geq 0)$ then it is unstable.

(ii) When the eigenvalues are negative $(\lambda_1, \lambda_2 \leq 0)$ then it is stable.

3.3.3 Complex eigenvalues

(i) When the real part of eigenvalues are both positive eg: $2 \pm 5i$. The phase plot is an unstable spiral.

(ii) When the real part of eigenvalues are both negative eg: $-3 \pm 4i$. The plot is a stable spiral.

(iii) When the real part is zero eg: $0 \pm 3i$. The eigenvalues are purely imaginary.

The next section explores the three main types of dynamical systems and looks at their respective phase plots.

3.4 Time independent systems

They are systems of ordinary differential equations which do not depend on the independent variable which is time. They are also referred to as autonomous systems. In this section, we would consider a system in R^n before looking at cases in R^2. These collection of equations may be written in the form

$$\begin{cases} x_1^{'} = V_1\left(x_1, x_2, \cdots x_n\right) \\ x_2^{'} = V_2\left(x_1, x_2, \cdots x_n\right) \\ x_3^{'} = V_3\left(x_1, x_2, \cdots x_n\right) \\ \qquad\vdots \\ x_n^{'} = V_n\left(x_1, x_2, \cdots x_n\right). \end{cases} \tag{3.2}$$

The autonomous equations (3.2) can also be represented in the form

$$\mathbf{x} = \begin{bmatrix} x_1 \\ x_2 \\ \vdots \\ x_n \end{bmatrix} \text{ and } \quad \mathbf{v} = \begin{bmatrix} V_1 \\ V_2 \\ \vdots \\ V_n. \end{bmatrix}$$

Therefore generalizing equation (3.2) gives

$$\mathbf{x}^{'} \quad = \quad V(\mathbf{x}). \tag{3.3}$$

The next section introduces some examples of autonomous systems and their general solutions.

Example 3.4.1. Consider a differential equation of the form: $ax'' + bx' + c(x) = f(t)$. The equation is a linear non-homogeneous second order ODE. The equation is said to be homogeneous if $f(t) = 0$. The equation above can be represented as a linear system of equations:

$$\begin{cases} x' = y \\ y' = -\frac{c}{a}x - \frac{b}{a}y. \end{cases} \tag{3.4}$$

Where equation 3.4 can also be expressed as a matrix of the form:

$$\begin{pmatrix} x' \\ y' \end{pmatrix} = \begin{pmatrix} 0 & 1 \\ \frac{-c}{a} & \frac{-b}{a} \end{pmatrix} \begin{pmatrix} x \\ y \end{pmatrix} \tag{3.5}$$

For example, we want to consider the general solution of the equations: $x''+2x'-3x = 0$. The equation can be written as a linear system of equations just as in (3.4) where $a = 1$, $b = 2$ and $c = -3$:

$$\begin{cases} x' = y \\ y' = 3x - 2y \end{cases} \tag{3.6}$$

Using the matrix method, equation 3.6 is given as:

$$\begin{pmatrix} x' \\ y' \end{pmatrix} = \begin{pmatrix} 0 & 1 \\ 3 & -2 \end{pmatrix} \begin{pmatrix} x \\ y \end{pmatrix} \tag{3.7}$$

The eigenvalues of the matrix would be determined by the determinant of the matrix.

$$\begin{vmatrix} -\lambda & 1 \\ 3 & -2-\lambda \end{vmatrix} = 0 \tag{3.8}$$

Therefore we have the characteristic equation given as

$$\lambda^2 + 2\lambda - 3 = 0 \tag{3.9}$$

The eigenvalues obtained by solving the equation 3.9 are given as $\lambda_1 = -3$ and $\lambda_2 = 1$. Since the eigenvalues are real and distinct, the eigenvectors are linearly independent. Therefore, we determine the eigenvectors associated to each eigenvalue by substituting the eigenvalues into equation 3.8. For $\lambda_1 = -3$

$$\begin{pmatrix} 3 & 1 \\ 3 & 1 \end{pmatrix} \begin{pmatrix} x \\ y \end{pmatrix} = \begin{pmatrix} 0 \\ 0 \end{pmatrix} \tag{3.10}$$

From equation 3.10 we have the expression $3x + y = 0$ in both cases. Let the value of $x = 1$, the eigenvector is given as $\begin{pmatrix} 1 \\ -3 \end{pmatrix}$. Using the same approach, the eigenvector for $\lambda = 1$ is $\begin{pmatrix} 1 \\ 1 \end{pmatrix}$. The general solution is of the form $C_1 \exp(\lambda_1 t) x_0 + C_2 \exp(\lambda_2 t) x_0$. Substituting the values of the eigenvectors and eigenvalues results in

$$X(t) \quad = C_1 \exp(-3t) \begin{pmatrix} 1 \\ -3 \end{pmatrix} + C_2 \exp(t) \begin{pmatrix} 1 \\ 1 \end{pmatrix} \tag{3.11}$$

Where C_1 and C_2 represent the arbitrary constants and they can be determined for given initial conditions. The phase plot is given below.

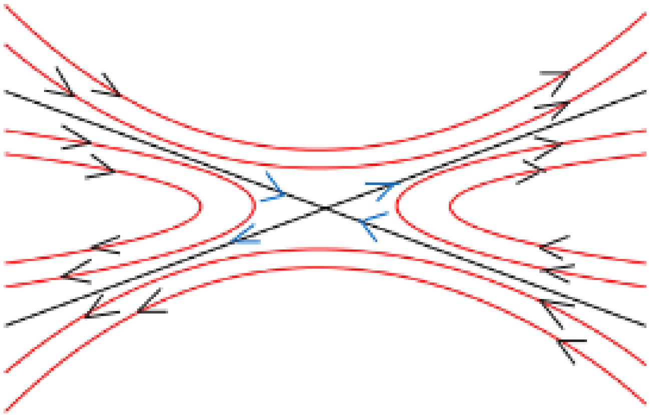

Figure 3.1: A Saddle

From figure (3.1), the black lines denote the separatrices and the red curves represent the trajectories of the solutions. The blue arrows on the separatrices indicate the direction of the separatrix. The separatrix with the blue arrows converging to the centre is the stable manifold and it is obtained from $\lambda = -3$. This is the point where trajectories moving towards the origin experience stability.Also $\lambda = 1$ results in the separatrix with the blue arrows diverging from the centre. It is referred to as the unstable manifold and trajectories moving towards these points experience instability. Futhrmore, the stable manifold(stability) and unstable manifold(instability) occur as $t \to -\infty$ and $t \to \infty$ respectively. From (3.1) it is observed that the manifolds determine the behaviour of the solutions represented as red curves as they move towards the centre.

Example 3.4.2. Consider another system of differential equations written in matrix form as:

$$\mathbf{x}^{'} = \begin{pmatrix} -3 & -2 \\ 5 & -1 \end{pmatrix} \mathbf{x} \tag{3.12}$$

Let A represent the matrix in 3.12 and determine the eigenvalues of the Matrix A. The determinant is given as

$$\begin{vmatrix} -3-\lambda & -2 \\ 5 & -1-\lambda \end{vmatrix} = 0 \tag{3.13}$$

The characteristic equation of 3.13 is given as

$$\lambda^2 + 4\lambda + 13 = 0.$$

The complex eigenvalues are given as $\lambda = -2 \pm 3i$. Since the complex roots are conjugates of each other, the eigenvectors are the same for both eigenvalues. The eigenvector associated with the eigenvalue is defined by the linear system $Ax = \lambda x$ where A is a square matrix, λ is a complex eigenvalue of A and x represents a vector. Therefore we select $\lambda = -2 + 3i$.

$$\begin{pmatrix} -1-3i & -2 \\ 5 & 1-3i \end{pmatrix} \begin{pmatrix} x \\ y \end{pmatrix} = \begin{pmatrix} 0 \\ 0 \end{pmatrix} \tag{3.14}$$

The eigenvector is given as $\begin{pmatrix} 2 \\ -1-3i \end{pmatrix}$ and

the solution of the equation is given as

$$\mathbf{x}' = \exp\left[(-2+3i)\, t\right] \begin{pmatrix} 2 \\ -1-3i \end{pmatrix} \tag{3.15}$$

The Euler formula is applied to equation 3.15 to separate it into real and imaginary parts.

$$\mathbf{x}' = \exp(2t) \left[(\cos 3t + i \sin 3t) \begin{pmatrix} 2 \\ -1-3i \end{pmatrix} \right]$$

$$\mathbf{x}' = \exp(2t)\left[\begin{pmatrix} 2\cos(3t) \\ -\cos(3t) + 3\sin(3t) \end{pmatrix}\right] + i\exp(2t)\left[\begin{pmatrix} 2\sin(3t) \\ -\sin(3t) - 3\cos(3t) \end{pmatrix}\right] \tag{3.16}$$

Let $V_1(t)$ represent the real part given as

$$\mathbf{V}_1(t) = \left[\begin{pmatrix} 2\cos(3t) \\ -\cos(3t) + 3\sin(3t) \end{pmatrix}\right] \tag{3.17}$$

and $V_2(t)$ represent the imaginary part given as

$$\mathbf{V}_2(t) = \left[\begin{pmatrix} 2\sin(3t) \\ -\sin(3t - 3\cos(3t)) \end{pmatrix}\right] \tag{3.18}$$

The general solution is a linear combination of the real and imaginary parts and it is given as

$$X_G = C_1\exp(-2t)\mathbf{V}_1(t) + C_2\exp(-2t)\mathbf{V}_2(t).$$

The phase portrait is given below.

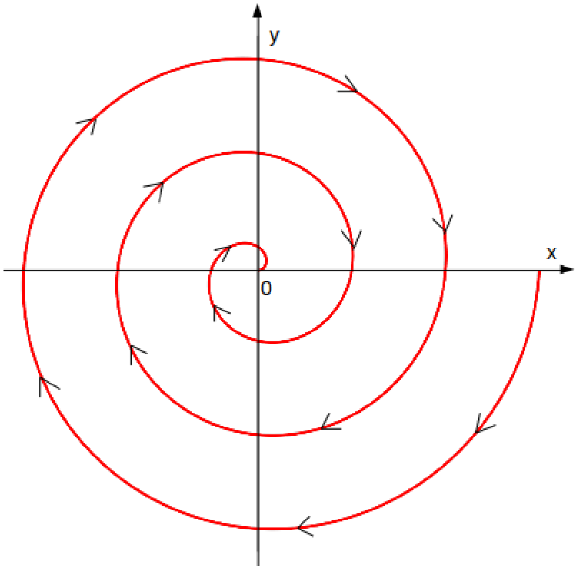

Figure 3.2: A stable spiral

In figure (3.2), the red continuous curves represents the spiral and the black arrows on the red curves depicts the direction of the behaviour of solutions of the system. Since the real parts of both eigenvalue are negative, the trajectories generated will converge towards the origin as $t \to \infty$. Therefore, the phase plot is a stable spiral.

Example 3.4.3. Consider a nonlinear autonomous system given as

$$\begin{cases} f(x,y) = x\,(3-x-2y) \\ g(x,y) = y\,(2-x-y) \end{cases} \tag{3.19}$$

We want to find the equilibrium points and determine the nature solutions of the system, and plot the possible phase portrait of the system.

Since it is a non-linear system, we compute for the fixed points of the system. The fixed points are obtained by setting the right hand sides of equation 3.19 to zero. This condition is used to determine all the fixed points. The first fixed point when both values of x and y are zero is $(0,0)$. When $x=0$, the fixed point is given as $(0,2)$. Also when $y=0$, the fixed point is $(3,0)$. Finally when both x and y are non-zero the fixed point is $(1,1)$.

The next step involves determining the linear stability of the fixed point by computing the Jacobian of the non-linear system. The Jacobian is given as:

$$J = \begin{vmatrix} \frac{df}{dx} & \frac{df}{dy} \\ \frac{dg}{dx} & \frac{dg}{dy} \end{vmatrix} = \begin{vmatrix} 3-2x-2y & -2x \\ -y & 2-x-2y \end{vmatrix} \tag{3.20}$$

The eigenvalues of the matrix in 3.20 is determined by substituting the values of the fixed points into the equation and solving the characteristic equation for each point.

When $(f\,(x,y), g(x,y)) = (0,0)$ the matrix in 3.20 results in

$$J = \begin{pmatrix} 3 & 0 \\ 0 & 2 \end{pmatrix} \tag{3.21}$$

The characteristic equation is given as $\lambda^2 - 5\lambda + 6 = 0$. The eigenvalues are $\lambda = 3$ and $\lambda = 2$ and the corresponding eigenvector are $\begin{pmatrix} 0 \\ 1 \end{pmatrix}$ and $\begin{pmatrix} 1 \\ 0 \end{pmatrix}$. Since both eigenvalues are real positive and distinct, $(0,0)$ is an unstable node for the linearised system and hence, by the linearisation theorem, also for non-linear systems.

For $(f(x,y), g(x,y)) = (0,2)$ the matrix 3.20 becomes

$$J = \begin{pmatrix} -1 & 0 \\ -2 & -2 \end{pmatrix} \tag{3.22}$$

The characteristic equation is $\lambda^2 + 3\lambda + 2$. The eigenvalues are $\lambda = -1$ and $\lambda = -2$

and the eigenvectors are $\begin{pmatrix} 0.4472 \\ -0.8944 \end{pmatrix}$ and $\begin{pmatrix} 0 \\ 1 \end{pmatrix}$. Both eigenvalues are real negative and distinct, therefore $(0, 2)$ is a stable node for the linearised system and likewise for the non-linear.

When $(f(x, y), g(x, y)) = (3, 0)$ the matrix 3.20 gives

$$J = \begin{pmatrix} -3 & -6 \\ 0 & -1 \end{pmatrix} \tag{3.23}$$

The characteristic equation is $\lambda^2 + 4\lambda + 3 = 0$. The eigenvalues are $\lambda = -3$ and $\lambda = -1$ and their corresponding eigenvectors are $\begin{pmatrix} 1 \\ 0 \end{pmatrix}$ and $\begin{pmatrix} -0.9487 \\ 0.3162 \end{pmatrix}$ The fixed point $(3, 0)$ is also a stable node.

Finally for $(1, 1)$, 3.20 results in

$$J = \begin{pmatrix} -1 & -2 \\ -1 & -1 \end{pmatrix} \tag{3.24}$$

The characteristic equation is given as $\lambda^2 + 2\lambda - 1 = 0$. The complex eigenvalues are given as $\lambda = -1 \pm \sqrt{2}i$ and the eigenvectors are given as $\begin{pmatrix} 0.8165 \\ -0.5774 \end{pmatrix}$ and $\begin{pmatrix} 0.8165 \\ -0.5774 \end{pmatrix}$. The point $(1, 1)$ is a stable spiral for the linearised system and hence, by linearisation theorem, also for the non-linear systems.

Figure 3.3 represents the phase portrait of equation 3.19. From the figure, the points $(0, 2)$ and $(3, 0)$ are the stable nodes and they are represented by the shaded circles. Also, the points $(0, 0)$ and $(1, 1)$ are denoted by circular rings and they are the unstable nodes. It is observed that the trajectories of the unstable nodes converge towards the stable points. Finally, the point $(1, 1)$ acts like the saddle in figure (3.1).

3.5 Time-Periodic systems

Time periodic systems are differential equations that depend explicitly on time and have their solutions recurring after a period of time (T). Subsequent solutions are given at $2T$, $3T$ and etc. The phase portrait of these systems displays vividly the repetitive behaviour of their solutions over time. Furthermore, their phase portrait are mostly closed orbits in phase plane and continuous curves. They are generally

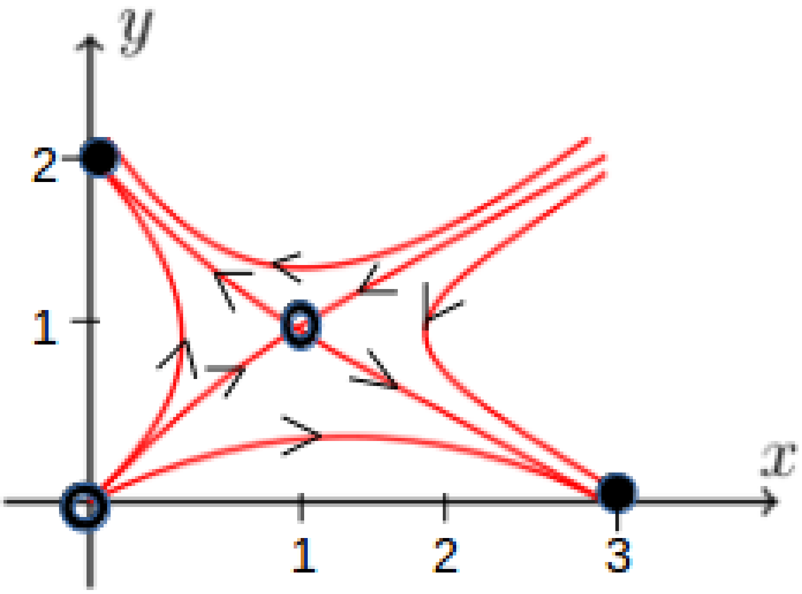

Figure 3.3: A Phase portrait of the non-linear time-independent dynamical system.

expressed as

$$\mathbf{x}^{'} = v(t, x) \tag{3.25}$$

Time-periodic systems are obtained from physical, chemical and biological systems that exhibit self-sustained oscillations. Some examples are the predator-prey model, the harmonic equation and the simple pendulum. The last example would be expatiated on because it would be beneficial in understanding the concept of boundaries in time-dependent systems.

Example 3.5.1. Consider the second order equation given below

$$x'' + x^3 = 0.$$

The equation is expressed as a first-order equation.

$$\begin{cases} x' = y \\ y' = -x^3 \end{cases} \tag{3.26}$$

Employing the method of separation of variables, equation (3.26) is solved as shown below.

$$
\begin{aligned}
\frac{dy}{dx} &= \frac{-x^3}{y} \\
ydy &= -x^3 dx
\end{aligned}
$$

Integrating both sides results in

$$
\begin{aligned}
\int ydy &= -\int x^3 dx \\
y^2 &= -\frac{x^4}{2} + 2C
\end{aligned}
$$

Hence the general solution is given as

$$y = \pm\sqrt{2}\left(C - \frac{x^4}{4}\right)^{\frac{1}{2}} \tag{3.27}$$

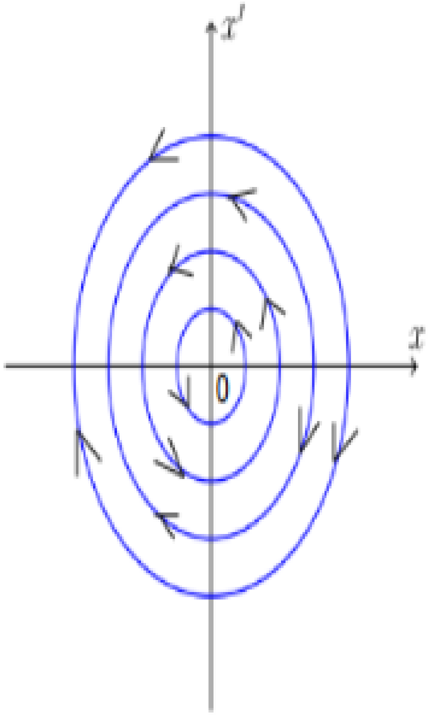

Figure 3.4: An Ellipse

In figure (3.4), the blue elliptical curves represent the solutions of the system. The black arrows on (3.4) denote the direction of the solutions of the periodic system. The phase plot is an ellipse.

Example 3.5.2. Consider the simple pendulum with the equation given as

$$x'' + \sin x = 0.$$

The second order differential equation is expressed as a first-order of the form

$$\begin{cases} x' = y \\ y' = -\sin x \end{cases} \tag{3.28}$$

The general solution is determined using the method of separation.

$$\frac{dy}{dx} = \frac{-\sin x}{y}$$
$$ydy = -\sin x dx$$

Both sides of the equation are integrated and the general solution of equation (3.28) is given as

$$y = \pm\sqrt{2}\,(\cos x + c)^{\frac{1}{2}} \tag{3.29}$$

The arbitrary constant c represents the parameter of the phase paths and it determines the nature of the phase plots. For values of c that lie between $-1 \leq c < 1$, the phase plot generates closed circular orbits. Also, when $c = 1$, the phase plot produces curves which are fixed at the equilibrium points. When $c > 1$ the phase plots are open orbits with a whirl-like motion.

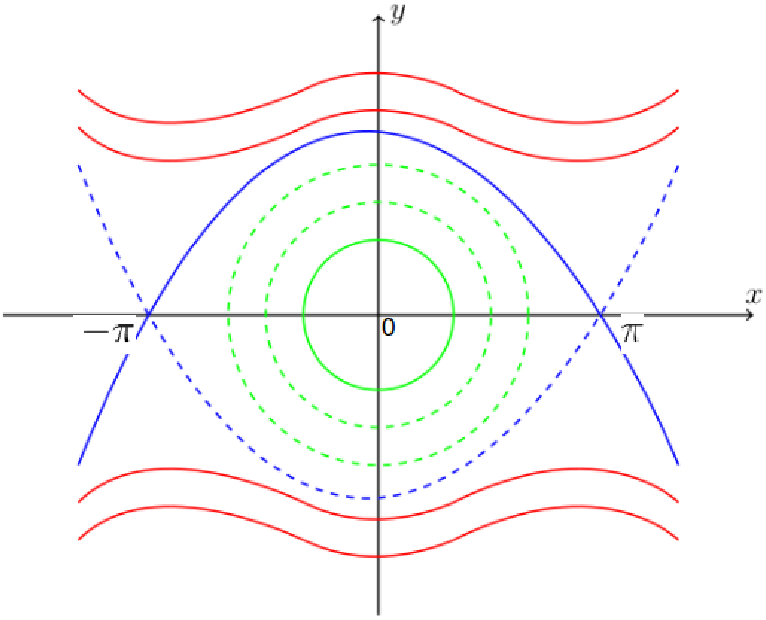

Figure 3.5: Phase plot of a simple pendulum

Figure 3.5 displays the phase portrait of a simple pendulum where the green circles represent closed paths, the separatrices are also represented as the blue curves and the red curves depict the whirling motion. The blue curves, just as the separating lines in the saddle plot, act as the unstable and stable manifold. They are given at the points $(0, 0)$ and $(\pm\pi, 0)$. Therefore in the separatrix(blue curves), the pendulum can only swing back and forth. As a result, the phase portrait of the solutions are circles. Also, outside the boundary, the pendulum moves in one direction. Correspondingly, the phase plots of solution are in a whirl-like form. Altogether the simple pendulum example provides adequate information in understanding hyperbolicity in dynamical systems.

3.6 Time-dependent systems

They are dynamical systems that depend explicitly on time, however unlike the time periodic systems, their solutions are not recurring. Most realistic dynamical systems such as the logistic growth equation and the movement of fluids are classified under this category. They are also referred to as non-autonomous systems and they are given as

$$\mathbf{x}' = \mathbf{v}\,(t, x) \tag{3.30}$$

The logistic growth equation would be solved below and the phase plot would be generated.

Example 3.6.1. Consider the differential equation given as

$$\frac{dP}{dt} = kP\left(1 - \frac{P}{k}\right) \tag{3.31}$$

The above equation is often used to model population growth in living organisms.

Using the method of separation of variables, the equation is given as

$$\int \frac{dP}{P\left(1 - \frac{P}{k}\right)} \quad = \quad \int kdt \quad \text{where } P \neq 0 \text{ and } P \neq K$$

Where the initial part of the equation is expressed as a partial fraction as shown below

$$\begin{aligned}
\frac{1}{P\left(1 - \frac{P}{k}\right)} &= \frac{1}{P} + \frac{1}{(k-P)} \\
\int \frac{dP}{P} + \int \frac{dP}{(k-P)} &= \int kdt \\
\ln(P) - \ln(k-P) &= kt + c \\
\ln\left(\frac{k-P}{P}\right) &= -kt - c \\
\frac{k-P}{P} &= \exp\left(-kt - c\right) \\
&= A\exp\left(-kt\right) \quad \text{where } A = \exp(-c)
\end{aligned}$$

The solution is given as

$$P\,(t) \quad = \quad \frac{k}{1 + A\exp(-kt)} \tag{3.32}$$

From the general solution, we compute for the initial population which is given as P_0.

$$P(0) \quad = \quad \frac{k}{1 + A\exp(-k(0))} = \frac{k}{1 + A} \tag{3.33}$$

Substituting equation 3.33 into equation 3.32, the general solution for the logistic growth equation in terms of P_0 is given as

$$P(t) = \frac{k}{1+\left(\dfrac{k-P_0}{P_0}\right)\exp(-kt)} \tag{3.34}$$

The equilibrium points of the logistic growth equation is obtained by equating (3.31) to zero. These points are $P = 0$ and $P = k$.

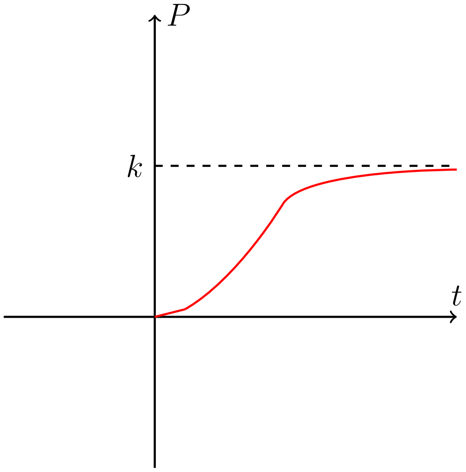

Figure 3.6: A phase plot of the logistic growth equation

From figure (3.6), the red sigmoid shaped curve represent the logistic growth curve. It can be observed that there is no growth when the time is zero. The dashed-lines represents the carrying capacity which serves as a boundary. The carrying capacity is defined as the maximum population size of organisms that the environment can sustain. It can be observed that the population grows gradually until it gets to the carrying capacity (k) where it maintains the same value after a period of time till it decreases. Therefore, the population cannot exceed the carrying capacity. This is an example of a dependent system where the population growth or the solution can be determined at any point in time.

However, to determine the behaviour of most time dependent systems is cumbersome because the solution of the differential equation varies with time. In some of these systems, there are regions of dynamically distinct behaviour which are presumed to be partitioned by separatrices. An example is the movement of fluids. Nonetheless, the distinct regions change with time likewise the separatrices. For fluid, even when the velocity field is of a simple form, the behaviour of the corresponding trajectories of the fluid can be complicated and seemingly unpredictable, an event called chaotic transport [24].

3.7 Lagrangian Coherent Structures(LCSs)

LCSs are defined as distinguished surfaces of trajectories in a dynamical system that exert a major influence on nearby trajectories over a time interval of interest[10]. Also, [25] defined LCSs as mobile separatrices that divide the flow into regions of qualitatively different dynamics. In steady flows such as time independent and time-periodic flows, the stable and unstable manifolds provide concrete information about the flow based on the critical points and the separatrices. However, for unsteady flows such as time dependent flows, the critical points and separatrices changes even within a short time interval making it difficult to determine the flow of tracer particles. Therefore, the LCSs acts as boundaries within the flow that prevents cross-mixing of fluid particles that exhibit different dynamical behaviours. Furthermore, they are embedded in the flow as well defined curves and they shape the flow of tracer particles by two major approaches namely attraction and repulsion. The LCSs can be referred to as attracting structures when time (T) is less than zero and they are important in studying transport of tracer particles in time-dependent systems. Also when $T < 0$, we have more attracting structures in the simulated flow. When $T > 0$, the LCSs is referred to as repelling LCSs and particles on opposite sides of these structures would separate from each other in the flow [25]. They are very useful in studying mixing in flows and therefore identifying these structures is key in understanding how flows separate in time-dependent systems. The attracting and repelling LCSs are collectively referred to as hyperbolic structures. Although coherent structures are ubiquitous in time-dependent flows, there is no well-defined mathematical theory for computing them in non-autonomous systems.

3.7.1 LCSs as material lines and surfaces

LCSs are hyperbolic material surfaces/lines in 2D flows and they can be visualised as continuous and smooth curves that shape the movement of fluid particles in a simulated flow[11]. They are time-evolving material surfaces along which passive tracers (e.g. dye,temperature, or any material which does not interact with the flow) develop distinct patterns exceeding typical time scales in the flow [8]. [11] proposed a mathematical definition for material lines and surfaces in the study of unsteady flows. The definition is given below.

Definition 3.7.2. Consider a $2D$ velocity field given as

$$\frac{dx}{dt} = u\left(x, t\right) \quad \text{with finite time interval} \quad [t_{int}, t_{fin}] \tag{3.35}$$

where t_{int} and t_{fin} represent the backward integration time and forward integration time respectively. The trajectories of the particles are represented as $x(t)$ and they are obtained from the $2D$ velocity field equation. In fluid mechanics, particle trajectories are referred to as path-lines and they can be observed as smooth curves on the x-axis. Therefore, a curve with initial conditions given as τ_0 when advected by the velocity field for a period of time t which represents all values of time, the conditions of the curve transforms into τ_t. The current conditions τ_t of the curve represent the material lines. The advection of particle trajectories from an initial position (x_0) at (t_{int}) to a later position in the flow at time (t_{fin}) is called a flow map. The flow map is mathematically given as

$$\Theta_{t_{int}}^{t_{fin}} : x_0 \to X\left(t_{fin}; t_{int}, x_0\right) \quad \text{where } x_0 \text{ represent the initial position}$$

When a deforming material line stretches over a $2D$ surface M in the (x,t) space, a material surface is formed [11].

3.7.3 Classifying LCSs as attracting or repelling material lines

This definition is based on LCSs being classified as material lines and it was proposed by [7].

Consider a material line $M(t)$ with time t, when it is advected by the flow map into a time-evolving material line $M(t)$, Then the flow map for $M(T) = \Theta_t^T M(t)$ with time interval $[t, T]$.

Let x represent a point on the material line such that $x \in M(t)$. Also let η denote the unit normal at x on $M(t)$ with the linearised flow map given as $\nabla\Theta_t^T(x)$. To be able to determine the behaviour of the material line $M(t)$ as it is advected in the flow, we determine the normal rate of repulsion. The normal rate of repulsion is defined as the projection of the linearised flow map $(\nabla\Theta_t^T(x))$ onto the normal (η) [15]. Therefore, we will denote it as $\beta_t^T(x, \eta)$ and it is perpendicular to the linearised flow map. Therefore, if $\beta_t^T(x, \eta) < 1$, it implies that $M(T)$ is overall attracting between $[t, T]$ along the trajectory starting from x. Subsequently, if $\beta_t^T(x, \eta) > 1$, then $M(t)$ is overall repelling between $[t, T]$ along the trajectory starting from x [7].

The figure below provides an illustration of how LCSs are identified in unsteady flows.

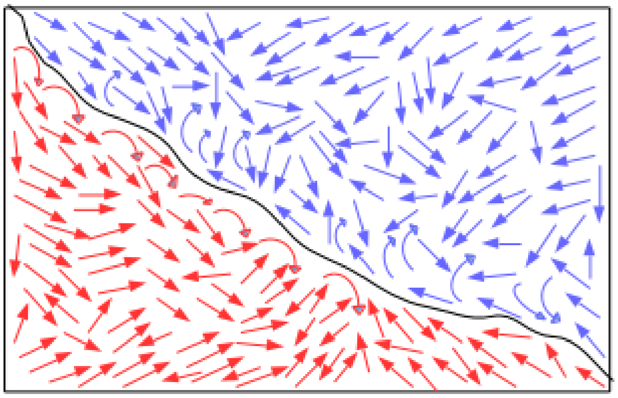

Figure 3.7: The trajectories of particles in an unsteady flow

From figure 3.7, the red and blue arrows denote particle trajectories of dynamically distinct properties and the thin black curve separating the particle trajectories represents the LCSs. We see that the movement of the trajectories in the flow is chaotic and could lead to mixing in fluids of the same properties. Here, trajectories of similar properties flow only within their specified domain and they don't mix with other particle trajectories of different properties. Furthermore, trajectories moving towards the boundary tend to bend inwards thus moving away from the LCSs. Therefore, the LCSs prevents cross-mixing of particle trajectories of different properties in the flow. Thereby acting as the invariant manifolds and critical points of steady flows.

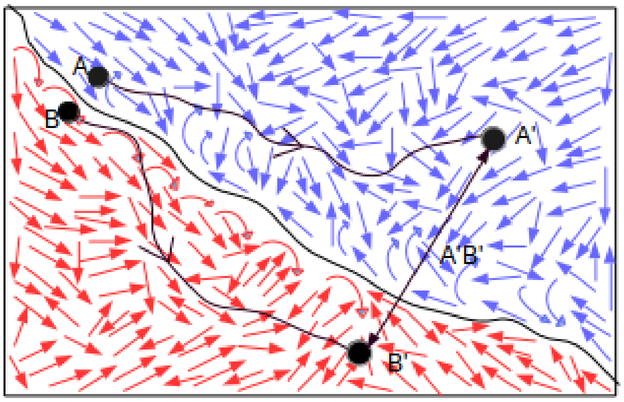

Figure 3.8: The trajectories of two particles with different dynamics in the flow

Figure 3.8, represents the advection of two particles at points A and B with initial time t in an unsteady flow. After some time interval, it is observed that the two points diverge from each other when it is integrated forward in time to new positions denoted as $A^{'}$ and $B^{'}$. A similar phenomena occurs when it is integrated backwards in time from the final position. In addition, the line $A^{'}B^{'}$ denotes the distance between the two points as they diverge from each other. The distance, separation or magnitude between the two points can be computed using the idea of a finite time Lyapunov exponent. The next section covers this in details.

Remark 3.7.4. We emphasize that these figures are only a schematic illustration to help explain the concept of LCSs and FTLE in fluid flows.

3.8 Finite Time Lyapunov Exponent(FTLE)

The finite time Lyapunov exponent is a scalar value which determines the amount of stretching/separation of the trajectories of particles when advected from an initial position $\mathbf{X} \in D$, where D is the domain, to a subsequent position $\mathbf{Y} \in D$ within a finite time interval $[t, t+T]$. The FTLE is a scalar value that varies as a function of space and time. For any given position in the flow, the maximum stretch at a finite time can be determined using the FTLE. The next section considers how the maximal stretch or the maximum FTLE is derived. In this section, vector values are represented in bold faces.

3.8.1 Maximum Stretch

Consider an arbitrary point $\mathbf{X} \in D$ at initial time $[t_0]$ and another point $\mathbf{Y} \in D$ very close to $\mathbf{X}$. The position of y is given as $\mathbf{Y} = \mathbf{X} + \delta\mathbf{X}(t_0)$ where $\delta\mathbf{X}(t_0)$ represents a perturbation of y from x. When these points are advected by the flow, the flow map of X and Y are represented as $\Theta_t^T(\mathbf{X})$ and $\Theta_t^T(\mathbf{Y})$ respectively. The two points diverge from each other with time. Therefore, to determine the maximum stretch of both points at final time (T), the flow map is given as

$$\delta\mathbf{X}(T) = \Theta_t^T(\mathbf{Y}) - \Theta_t^T(\mathbf{X})$$

where we can substitute the expression $\mathbf{Y} = \mathbf{X} + \delta\mathbf{X}(t)$ resulting in

$$\delta\mathbf{X}(T) \quad = \Theta_t^T\left(\mathbf{X} + \delta\mathbf{X}(t_0)\right) - \Theta_t^T\left(\mathbf{X}\right). \tag{3.36}$$

The right hand side of the equation above can be simplified by performing a Taylor series expansion as shown below.

$$\Theta_t^T\left(\mathbf{X} + \delta\mathbf{X}(t_0)\right) \quad = \Theta_t^T\left(\mathbf{X}\right) + \frac{d\Theta_t^T(\mathbf{X})}{d\mathbf{X}}\delta\mathbf{X}(t_0) + \frac{d^2\Theta_t^T(\mathbf{X})}{d\mathbf{X}^2}\delta\mathbf{X}(t_0)^2 + \ldots$$

Substituting this expression into equation 3.36 and applying the Landau notation to stand for the subsequent values of the expansion results in

$$\delta\mathbf{X}(T) \quad = \frac{d\Theta_t^T(\mathbf{X})}{d\mathbf{X}}\delta\mathbf{X}(t_0) + \mathcal{O}\left(\| \delta\mathbf{X}(t_0) \|^2\right) \tag{3.37}$$

However, the subsequent values of the expansion which are represented by the Landau notation are very small and therefore they are negligible. Therefore, equation 3.36 becomes

$$\delta \mathbf{X}(T) \quad = \tfrac{d\Theta_t^T(\mathbf{X})}{d\mathbf{X}} \delta \mathbf{X}(t_0) \tag{3.38}$$

Now because we are interested in determining the average stretching of the points, we compute for the magnitude.

$$\| \ \delta \mathbf{X}(T) \ \| \quad = \sqrt{\tfrac{d\Theta_t^T(\mathbf{X})}{d\mathbf{X}} \delta \mathbf{X}(t_0)} \tag{3.39}$$

Applying the idea of inner products, the above expression can be expressed as

$$\begin{aligned} \| \ \delta \mathbf{X}(T) \ \| \quad &= \sqrt{\Big\langle \tfrac{d\Theta_t^T(\mathbf{x})}{d\mathbf{X}} \delta \mathbf{X}(t_0), \tfrac{d\Theta_t^T(\mathbf{x})}{d\mathbf{X}} \delta \mathbf{X}(t_0) \Big\rangle} \\ &= \sqrt{\Big\langle \delta \mathbf{X}(t_0), \tfrac{d\Theta_t^T(\mathbf{X})}{d\mathbf{X}}^* \tfrac{d\Theta_t^T(\mathbf{X})}{d\mathbf{X}} \delta \mathbf{X}(t_0) \Big\rangle} \end{aligned}$$

From [24], $\frac{d\Theta_t^T(\mathbf{X})}{d\mathbf{X}}$ is a matrix which represents the derivatives of the flow map with respect to their variations from the initial position and $\delta X(t_0)$ is a vector. The matrix is given as

$$\frac{d\Theta_t^T}{d\mathbf{X}} = \begin{bmatrix} \frac{\partial \Theta_t^T(\mathbf{X}_1)}{\partial \mathbf{X}_1} & \frac{\partial \Theta_t^T(\mathbf{X}_1)}{\partial \mathbf{X}_2} & \cdots & \frac{\partial \Theta_t^T(\mathbf{X}_1)}{\partial \mathbf{X}_n} \\ \frac{\partial \Theta_t^T(\mathbf{X}_2)}{\partial \mathbf{X}_1} & \frac{\partial \Theta_t^T(\mathbf{X}_2)}{\partial \mathbf{X}_2} & \cdots & \frac{\partial \Theta_t^T(\mathbf{X}_2)}{\partial \mathbf{X}_n} \\ \vdots & \vdots & & \\ \frac{\partial \Theta_t^T(\mathbf{X}_n)}{\partial \mathbf{X}_1} & \frac{\partial \Theta_t^T(\mathbf{X}_n)}{\partial \mathbf{X}_2} & \cdots & \frac{\partial \Theta_t^T(\mathbf{X}_n)}{\partial \mathbf{X}_n} \end{bmatrix}$$

The deformation gradient is computed for the matrix and it is denoted as

$$\Delta \Theta_t^T(\mathbf{X}) \quad = \tfrac{d\Theta_t^T(\mathbf{X})}{d\mathbf{X}}^\star \tfrac{d\Theta_t^T(\mathbf{X})}{d\mathbf{X}} \tag{3.40}$$

where $\star$ represents the transpose and also the deformation gradient will give a symmetric matrix[24]. Now substitute equation 3.40 into the norm equation gives:

$$\| \ \delta \mathbf{X}(T) \ \| \quad = \sqrt{\langle \delta \mathbf{X}(t_0), \Delta \Theta_t^T(\mathbf{X}) \delta \mathbf{X}(t_0) \rangle} \tag{3.41}$$

Since we want to determine the maximum stretch in finite time, the equation above would be rewritten as

$$max_{\delta \mathbf{X}(t_0)} \parallel \delta \mathbf{X}(T) \parallel \ = \sqrt{\langle \delta \mathbf{X}(t_0), \Delta_{max} \Theta_t^T(\mathbf{X}) \delta \mathbf{X}(t_0) \rangle} \tag{3.42}$$

To obtain the maximum stretching, we use ideas from linear algebra and choose the initial position $\delta \mathbf{X}(t_0)$ to be aligned with the eigenvector corresponding to the maximum eigenvalue of $\Delta_{max}\Theta_t^T(\mathbf{X})$ such that:

$$\Delta_{max} \Theta_t^T(\mathbf{X}) \delta \mathbf{X}(t_0) \ = \lambda_{max} \Delta \delta \mathbf{X}(t_0)$$

Where $\lambda_{max}\Delta$ is the maximum eigenvalue that corresponds with $\Delta_{max}\Theta_t^T(\mathbf{X})$ and it is also associated with the vector $\bar{\delta}\mathbf{X}(t_0)$. Substituting the eigenvalue into the equation 3.42 results in:

$$max_{\delta \mathbf{X}(t_0)} \parallel \delta \mathbf{X}(T) \parallel \ = \sqrt{\langle \bar{\delta} \mathbf{X}(t_0), \lambda_{max} \Delta \bar{\delta} \mathbf{X}(t_0) \rangle} \tag{3.43}$$

Employing the concept of inner products where

$$\langle \mathbf{X}, A\mathbf{X} \rangle = A \langle \mathbf{X}, \mathbf{X} \rangle = A \parallel \mathbf{X} \parallel^2$$

Equation 3.42 can be given as

$$max_{\delta \mathbf{X}(t_0)} \parallel \delta \mathbf{X}(T) \parallel \ = \sqrt{\lambda_{max} \Delta \parallel \bar{\delta} \mathbf{X}(t_0) \parallel^2}$$

$$max_{\delta \mathbf{X}(t_0)} \parallel \delta \mathbf{X}(T) \parallel \ = \sqrt{\lambda_{max} \Delta} \parallel \bar{\delta} \mathbf{X}(t_0) \parallel \tag{3.44}$$

As defined in [24], the FTLE is given as

$$\sigma_t^T(\mathbf{X}) = \frac{1}{\mid T \mid} \log \sqrt{\lambda_{max} \left(\Delta \right)} \tag{3.45}$$

where T represent the final integration time. The integration time can be negative for backward integration and also positive for forward integration. This explains the role played by the absolute value sign in equation 3.45. Therefore, from equation 3.45,

$$\sqrt{\lambda_{max} \left(\Delta \right)} = \exp \left(\sigma_t^T(\mathbf{X}) \mid T \mid \right) \tag{3.46}$$

Substituting equation 3.46 into the equation 3.44, the maximum stretch between the two points in finite time is given by

$$Max_{\delta \mathbf{X}(t_0)} \parallel \delta \mathbf{X}(T) \parallel \ = \exp\left(\sigma_t^T(\mathbf{X}) \mid T \mid\right) \parallel \bar{\delta} \mathbf{X}(t_0) \parallel \tag{3.47}$$

3.8.2 Defining the LCSs as the second derivative of the FTLE

[24] proposed a definition for detecting LCSs in an FTLE field. This definition was based on the numerical computations of the FTLE fields which would be studied in Chapter 4. [24] defined LCSs as the second derivative of an FTLE field based on this explanation.

Definition 3.8.3. A second-derivative ridge of σ_t^T is an injective curve $c : (a, b)$ satisfying the following conditions for each $s \in (a, b)$:

SR1: The vectors $c'(s)$ and $\nabla \sigma_t^T \, (c(s))$ are parallel.

SR2: $\Sigma(n, n)= min_{\|u\|=1} \Sigma(u, u) < 0$ where n is a unit normal vector to the curve $c(s)$ and Σ is though of as a bilinear form evaluated at the point $c(s)$.

The ridges represent smooth curves in the unsteady flow and also the Hessian which is denoted as $\Sigma = \frac{d^2 \sigma_t^T(x)}{dx^2}$. Additionally, since σ_t^T varies with time we indicate the time on each curve $c(s)$ at which the σ_t^T is computed. eg: if the FTLE is computed at time t_1, $c(s)$ becomes $c_{t_1}(s)$.

Chapter 4

Numerical Simulations and Analysis

This chapter introduces a numerical approach of detecting LCSs with the FTLE method. Firstly, we carry out numerical simulations on two types of the double gyre motions namely: time-independent and time-dependent gyres. The numerical computations generate the velocity fields and the FTLE plots of both the time-independent and time-dependent flows. The double gyre provides suitable grounds for studying complex time dependent systems. The next section involves FTLE computations on ocean surface velocity fields of the West African Atlantic coast obtained from [1]. The main goal is to identify the LCSs and how they vary in time using realistic flow fields. Afterwards, a section of the data which covers the Gulf of Guinea is extracted for further analysis. The algorithm that computes the FTLE's of the ocean current velocity data is developed by [6] and it was employed on a double gyre example and a simulated flow in the Argentine basin. Initially, the algorithm loads the ocean current velocity data into the workspace. Then, it requests for the following parameters: the longitude, the latitude, the zonal and meridional velocities. Furthermore, the code requests values for the following: the total integration time, the time step, the zonal and meridional resolutions of the tracer grid, the method of integration, the direction of integration and the number of flow maps to generate. Finally, using [2], plots for the flow maps are developed. These steps are indicated in the sections on the double gyre example and the numerical computations of the FTLE.

4.1 Double gyre model

A gyre refers to any whirling mass of fluid (the point where the fluid flow revolves around an axis line) formed naturally in fluids. However, it is mostly studied in oceanography, where the wind velocity on the ocean surface causes a large system of circulating ocean currents to be formed. These systems act as transport barriers by separating fluid particles in a geophysical flow. A double gyre is formed when two counter-rotating gyres revolve around each other. Also, the double gyre model is a numerical representation of the double-gyre pattern that occurs mostly in geophysical flows. This model provides a practical way of understanding the FTLE and LCSs. It may be defined by the stream function

$$\Psi(x,y,t) \;=\; A\sin\left(\pi f(x,t)\right)\sin(\pi y) \tag{4.1}$$

$$\text{where} \quad \begin{cases} f\left(x,t\right) & = a(t)x^2 + b(t)x \\ a(t) & = \epsilon\sin(\omega t) \\ b(t) & = 1 - 2\epsilon\sin(\omega t) \end{cases} \tag{4.2}$$

where A represents the magnitude of the velocity vectors, ω is the frequency of oscillation and ϵ denotes the amplitude of the motion of the separation point. The effects of these parameters on the double gyre will be explained in later sections. The velocity fields of the trajectories of double gyre is obtained by differentiating equation 4.1 with respect with x and y respectively.

$$\begin{cases} U = \frac{-\partial\Psi}{\partial y} & = -\pi A\sin\left(\pi f(x,t)\right)\cos(\pi y) \\ V = \frac{\partial\Psi}{\partial x} & = \pi A\cos\left(\pi f(x)\right)\sin(\pi y)\frac{df}{dx} \\ \frac{df}{dx} & = 2\epsilon\sin(\omega t)\left[x-1\right]+1 \end{cases} \tag{4.3}$$

where U represent the zonal velocity(velocities along the coordinates of the x-axis) and V denotes the meridional velocity (velocities along the coordinates of the y-axis). The equations above will generate the trajectories of the gyre as well as depict the LCSs in the flow.

4.1.1 Computational method for the Double gyre

This section explains the steps taken in the numerical integration of the double gyre model. Firstly, we carry out numerical computations to determine the zonal and meridional velocities from equation 4.3. These velocities are computed over a cartesian grid with the x-axis(longitude) given as $[2, 0]$ and y-axis also given as $[0, 1]$. The parameter values given in equation 4.3 have major implications on the double gyre model. When the magnitude of the velocity vectors (A) is small the distance between the counter-rotating gyres and the boundary is minimized and vice-versa when it is large. Smaller values of A are preferred since it produces more refined curves close to the separatrix. Also, ω determines the frequency of oscillations throughout the integration time. More oscillations are completed for smaller frequency with larger integration time and conversely for large frequency in smaller integration time. Lastly, the value of ϵ controls the movement of the separatrix. A matlab function called quiver is used to plot the velocity vectors of the double-gyre. Also, to determine the FTLE fields, the Runge-Kutta algorithm developed by [2] is used to advect fluid particles from an initial position(x_0) at time(t) to a subsequent position $x(t+T; t, x_0)$ at time $t+T$. The algorithm advects the fluid particles by integrating the velocity dataset. Afterwards it computes for the spatial gradient by determining the finite difference for each point in the flow map. Finally, the Runge-Kutta algorithm determines the FTLE values (σ) at each point by substituting the gradient values into 3.45. This process is repeated for subsequent ranges of time. A matlab function called pcolor is used to plot the FTLE fields.

4.1.2 Time-independent double gyre

A time independent gyre is generated when ϵ is set to zero in equation 4.3. When $\epsilon = 0$, the separatrix remains fixed at the centre for the total integration time. The equations governing the flow are given by:

$$\begin{cases} U &= -\pi A \sin\left(\pi f(x)\right)\cos(\pi y) \\ V &= \pi A \cos\left(\pi f(x)\right)\sin(\pi y) \\ \frac{df}{dx} &= 1 \end{cases} \tag{4.4}$$

For the numerical simulations, a total integration time of 20 and a time step of 0.1 is selected. Also, the selected values of the parameters for the numerical computation of the double gyre are given as $A = 0.1$, $\epsilon = 0$ and $\omega = 2\pi/10$. These values are akin to the values used for the double gyre example in [24].

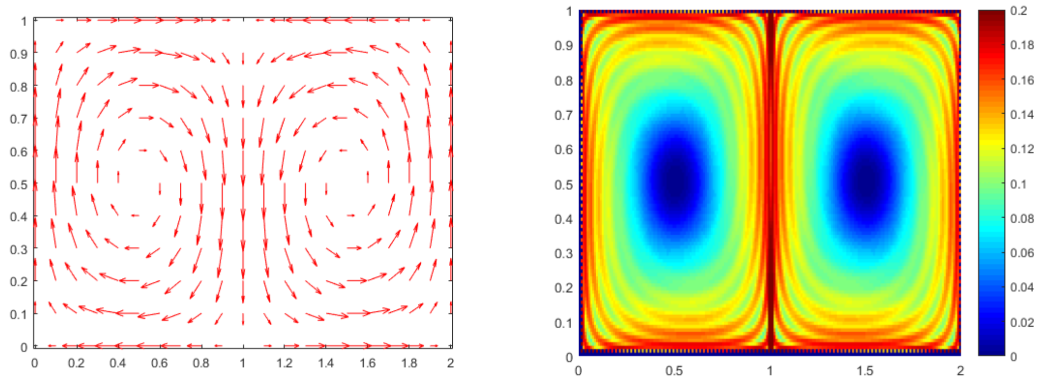

(a)

(b)

Figure 4.1: The plot of the trajectories of the velocity vectors and the FTLE plot respectively

Figure 4.1a, indicates the trajectories of the gyre moving in opposite directions separating the plot into two equal but dynamically distinct regions. Also, the gyres are separated at the points $[1, 0]$ and $[1, 1]$ by heteroclinical trajectories. Heteroclinical trajectories act as the separatrix by the dividing distinct regions in the flow. Since $\epsilon = 0$, the hetoroclinical trajectories remain fixed at the points $[1, 0]$ and $[1, 1]$ at all times. Figure 4.1b represent the $2D$ plot of the double gyre indicating the FTLE ridges in the flow. From the figure, the highest repelling LCSs are represented as red curves that lie on the separatrix. The magnitude of the FTLE values are shown on the colour-bar. There is a quick separation of fluid particles at this point in the flow.

4.1.3 Time-dependent double gyre

Time-dependent gyre occur when the value of (ϵ) is not zero in 4.3. For the computation of the time-dependent gyre, the parameter values used for the time independent gyre are maintained except ϵ which is given as 0.1. Also, the total integration time and the domain is maintained for the numerical simulations of the time-dependent double gyre. Furthermore, the intervals was increased from 0.1 to 5 to provide a clear view of the velocity vectors plots. Choosing a large interval for the velocity fields does not result in large errors. It produces the same result as that of a smaller interval. The only difference is that larger intervals give a more vivid representation of the numerical simulation as compared with the smaller intervals. The velocity vectors and the FTLE plots are shown below.

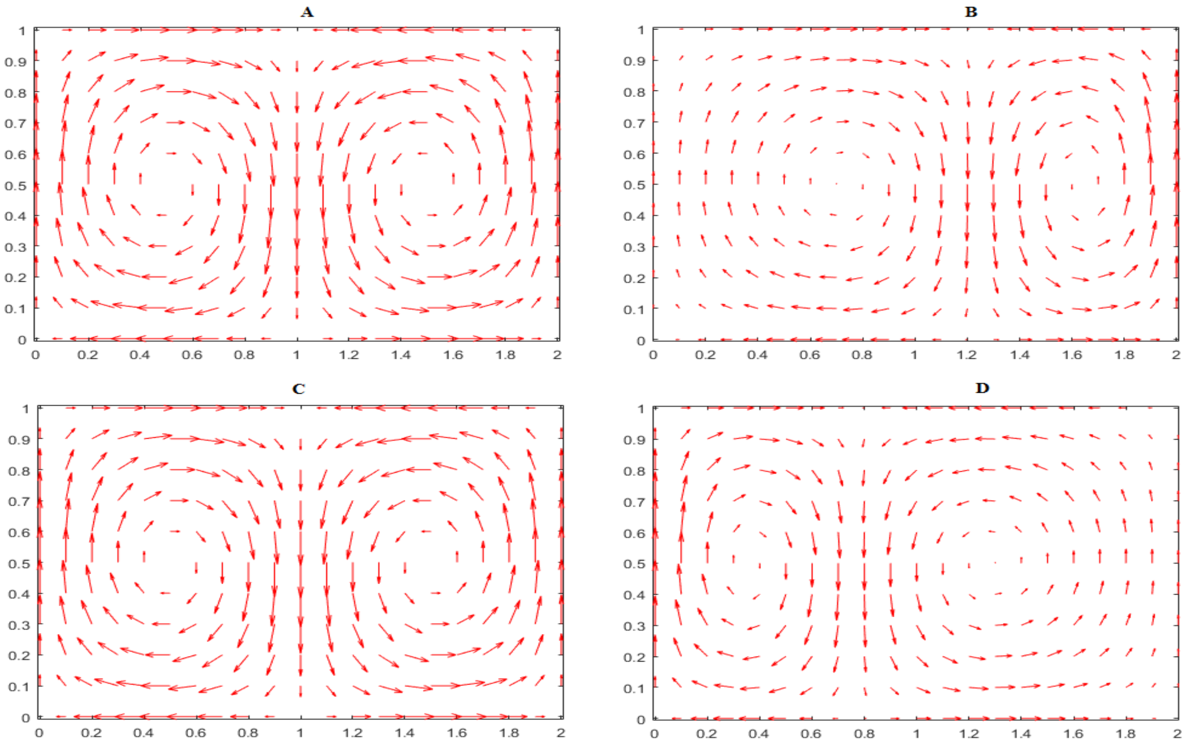

Figure 4.2: The plot of the trajectories of the double gyre at $t = 1$, $t = 3$, $t = 6$ and $t = 19$ respectively.

The figures show the velocity vectors of the double gyre at $t = 1$, $t = 3$, $t = 6$ and $t = 19$. Figure 4.2**A** is similar to what we see for the time independent double gyre case shown in figure 4.1**A**. The two gyres are of similar size with flows moving in opposite directions. In figure 4.2**B**, the position of the heteroclinical trajectories shift rightwards and they are fixed at the point $[1.2, 0]$ and $[1.2, 1]$. This causes the gyres to have distinct sizes with the initial gyre larger than the other gyre. Also, for figure 4.2**C**, the heteroclinical trajectories move back to the initial position as indicated in 4.2**A** and the gyres are of the same size. The time-dependent gyres are said to have completed a period at $t = 6$. This also occurs for $t = 12$ and $t = 18$. Therefore, the time-dependent double gyre completes 3 periods during the total integration time. Finally, in figure 4.2**D** the heteroclinical trajectories move leftwards to the position $[0.8, 0]$ and $[0.8, 1]$. Also, the gyres are of different sizes with the second gyre larger than the initial.

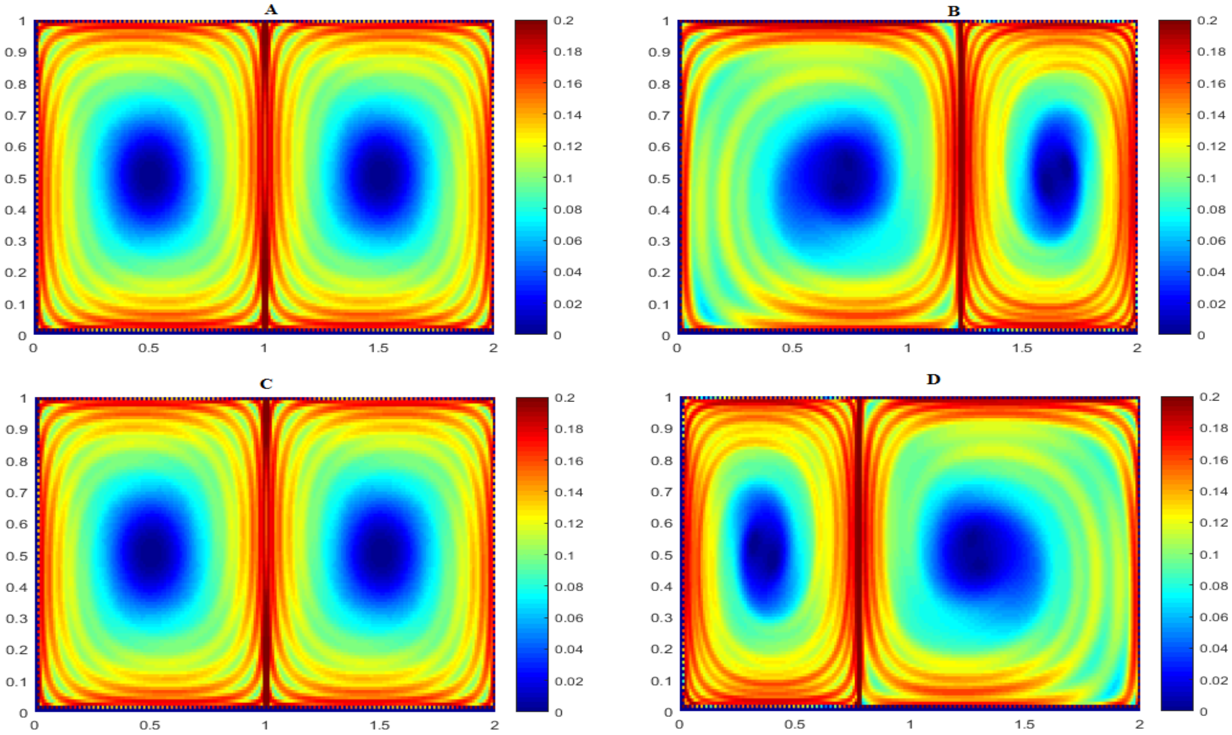

Figure 4.3: The FTLE plot at $t = 1$, $t = 3$, $t = 6$ and $t = 19$ respectively.

Figures 4.3**A**, 4.3**B**, 4.3**C** and 4.3**D** represent the corresponding FTLE field plots of the vector velocities given above. For all figures, it can be observed that the red curves represent the magnitude of the High FTLE values . They are given in the interval $[0, 0.2]$ on the colour-bar. At the position of the red curve, trajectories experience the quickest divergence in the flow. Therefore, the red curves represent the repelling LCSs as they divide the flow into two distinct regions. In addition, the magnitude of the Low FTLE values lie in the range $[0, 0.14]$ on the colour-bar. The rate of divergence of velocity vectors is reduced as you move down the colour-bar. Since the FTLE plots are in $2D$, the attracting and repelling LCSs can be visualized as material curves.

4.2 Numerical Computations of the FTLE on Satellite data

In this section, the importance of the LCSs acting as transport barriers would be demonstrated on a satellite data of the Atlantic Ocean. The data is obtained from [1] and it spans from 1^{st} October 2014 to 13^{th} June 2018. The data files are sorted from the initial date to the last date of data collection. Afterwards using a Matlab toolbox called Nctoolbox which provides read only access to common data model datasets, the parameters of the dataset are extracted. They consist of the depth, salinity, temperature, meridional velocity, height, time(t), longitude, latitude, zonal velocity and mixed layer depth. For our analysis, we only extract the velocities at the surfaces. The values of the meridional velocity (U), zonal velocity (V), latitude (lat), longitude (lon) and time(t) are extracted from the data using a Matlab code developed by [20]. The longitude and latitudes of the entire dataset is given as [-35°W,15°E] and [-9.8750°S,30.1250°N] respectively. The velocities are given as $3D$ matrices where the first, second and third dimension consists of the longitudes, latitudes and time. Similar to the double-gyre models, the Runge-Kutta algorithm is used to advect the fluid particles by integrating the velocities. Some other values that are important in the computational procedure are the total integration time, the time step of integration, the axis resolution and the direction of integration. The total integration time determines how long the fluid particles are advected in the flow. Longer time interval produces more refined LCSs in the flow. The time step of integration divides the total integration time to determine the next position of the fluid particles in the ocean flow. Also a finer resolution produces well refined LCSs. Furthermore, the numerical integration is either performed backward or forwards in time. Backward integration helps in determining the position from which a particle was advected over a given time step whiles the forward integration time computes for the position to which a particle will be advected during a time step. Finally, the Runge-Kutta algorithm is used to compute for a selected number of flow maps based on the values selected for the parameters and using a Matlab package produced by [2]. For the purposes of these project, we are mainly interested in observing the effect of the repelling LCSs on a simulated flow therefore we employ the backward time integration.

4.2.1 Velocity fields of the Atlantic Ocean

Just like the velocity fields of the double gyre models, the velocity plots of the satellite data reveal important details about the geophysical flow. It indicates the movement of fluid flows. Figures 4.4**A** and 4.4**B** represent the surface velocities in the Atlantic Ocean.

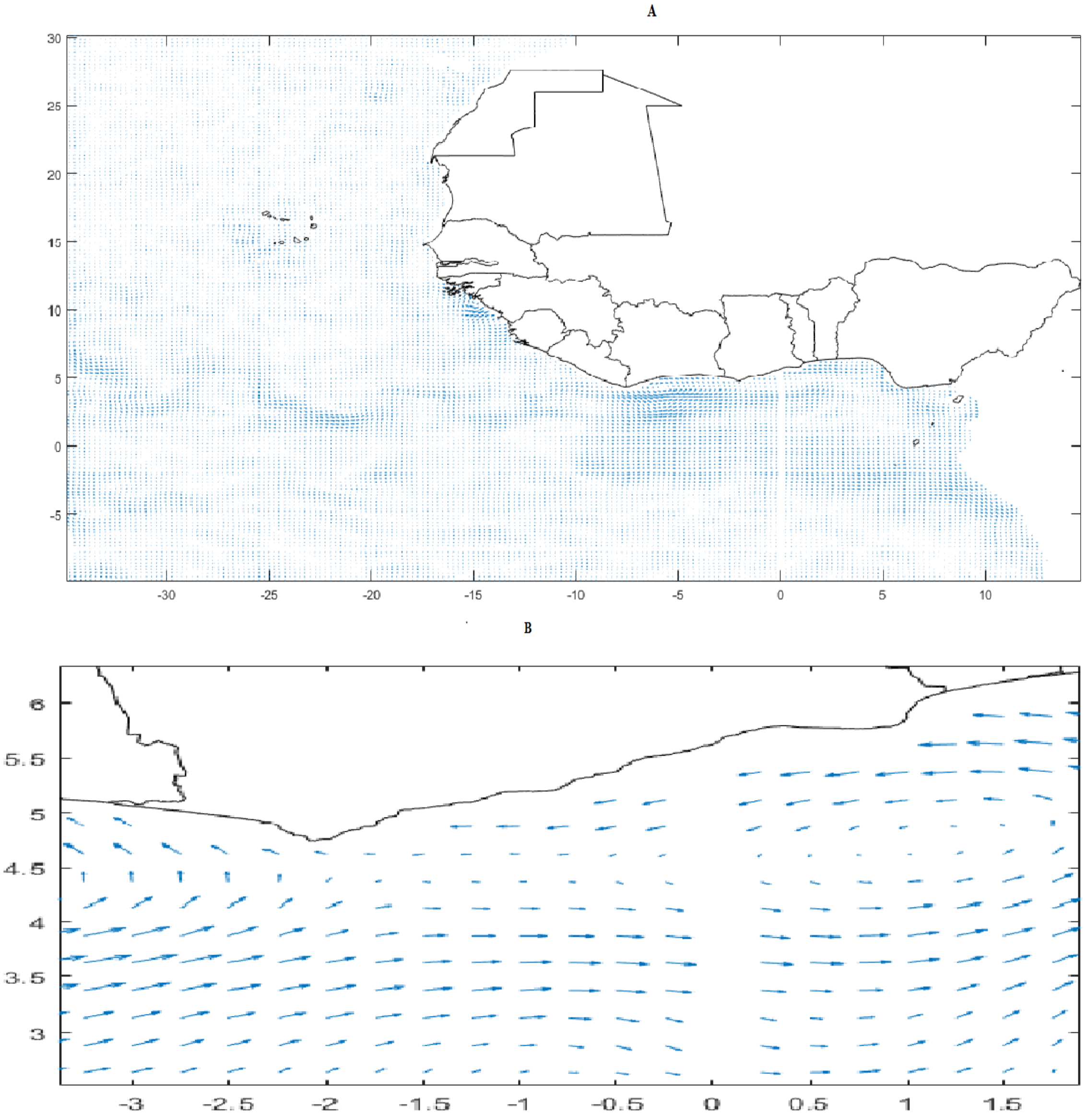

Figure 4.4: The surface velocity fields in **A** the Atlantic Ocean and **B** zoomed view of the velocity fields at Ghana's coastline respectively.

From figure 4.4**A**, the trajectories are represented as blue arrows and the white section of the figure represents the land mass of West African and parts of north Africa. Furthermore, figure 4.4**A** also indicates the land mass of countries along the Atlantic ocean such as Ghana, Cote d'ivoire, Liberia and a lot more. Figure 4.4**B** represents a enlarged section of figure 4.4**A**, specifically Ghana's coastline. However, our interest lies in the movement of fluid trajectories in the simulated flow which is clearly shown in figure 4.4**B**. In both diagrams, it can be observed that the fluid flows are exhibiting chaotic movement.

Remark 4.2.2. From figure 4.4**A**, there is a white straight line formed at longitude 0°; this is a defect in the satellite velocity data. This defect is also evident in all the FTLE fields plots in subsequent sections.

4.2.3 FTLE plots for Numerical Computations on the Atlantic Ocean

Figures 4.5a and 4.5b depict the evolution of the FTLE fields in the entire West Africa Atlantic coast. However only the first and last flow maps are plotted to give a clear representation of the evolution of the LCSs in the ocean flow. The resolution on the tracer grids for the satellite data is 0.25 and also the integration is performed backwards in time. The total time of integration and the time step used for 4.4 is maintained.

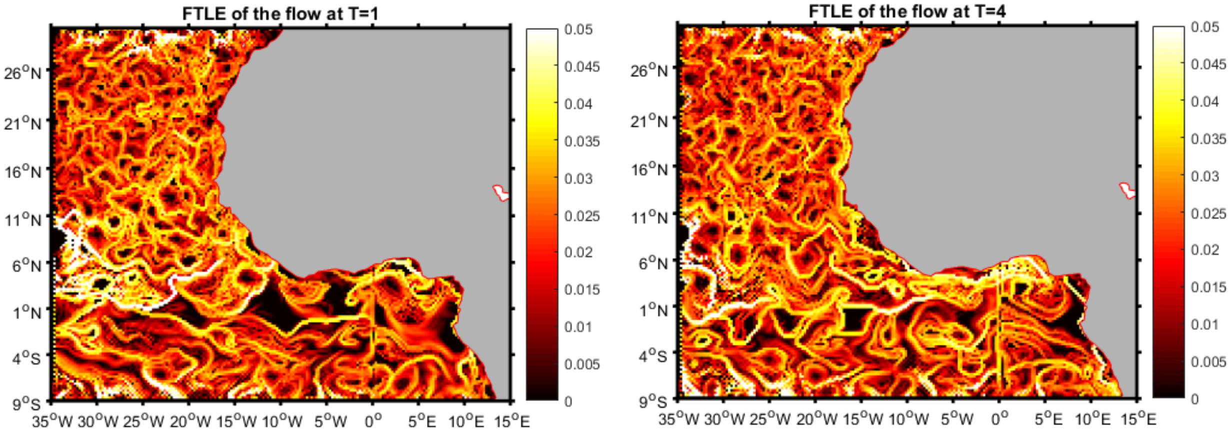

Figure 4.5: The FTLE fields of the Atlantic Ocean at $T = 1$ and $T = 4$ respectively.

In the figures, the wiggly lines in the plot represent the presence of numerous LCSs, and those that are whitish indicate the most repelling/attracting structures. From 4.5a there is a concentration of high repelling LCSs between longitude 30° and latitude 11° N. However, in 4.5b, there are few high repelling LCSs formed at the same point. We next zoom into the Gulf of Guinea to investigate the nature of the LCSs around the coast of Ghana.

4.3 LCSs in the Gulf of Guinea

The longitude and latitude lie in the range [-10°W,10°E] and [-6.25°S,6.125°N]. Six FTLE plots are generated for each total integration time given as: $T = 50$, $T = 70$ and $T = 100$. Also, the six FTLE plots represent the snapshot of the flow maps for the following time intervals: $T = 1$, $T = 5$, $T = 9$, $T = 13$, $T = 17$ and $T = 21$. This helps in giving a vivid view of the progression of the LCSs in the Gulf of Guinea. The resolution is 0.25 and it is maintained for all the integration times. In addition, computations were performed for backward time integration.

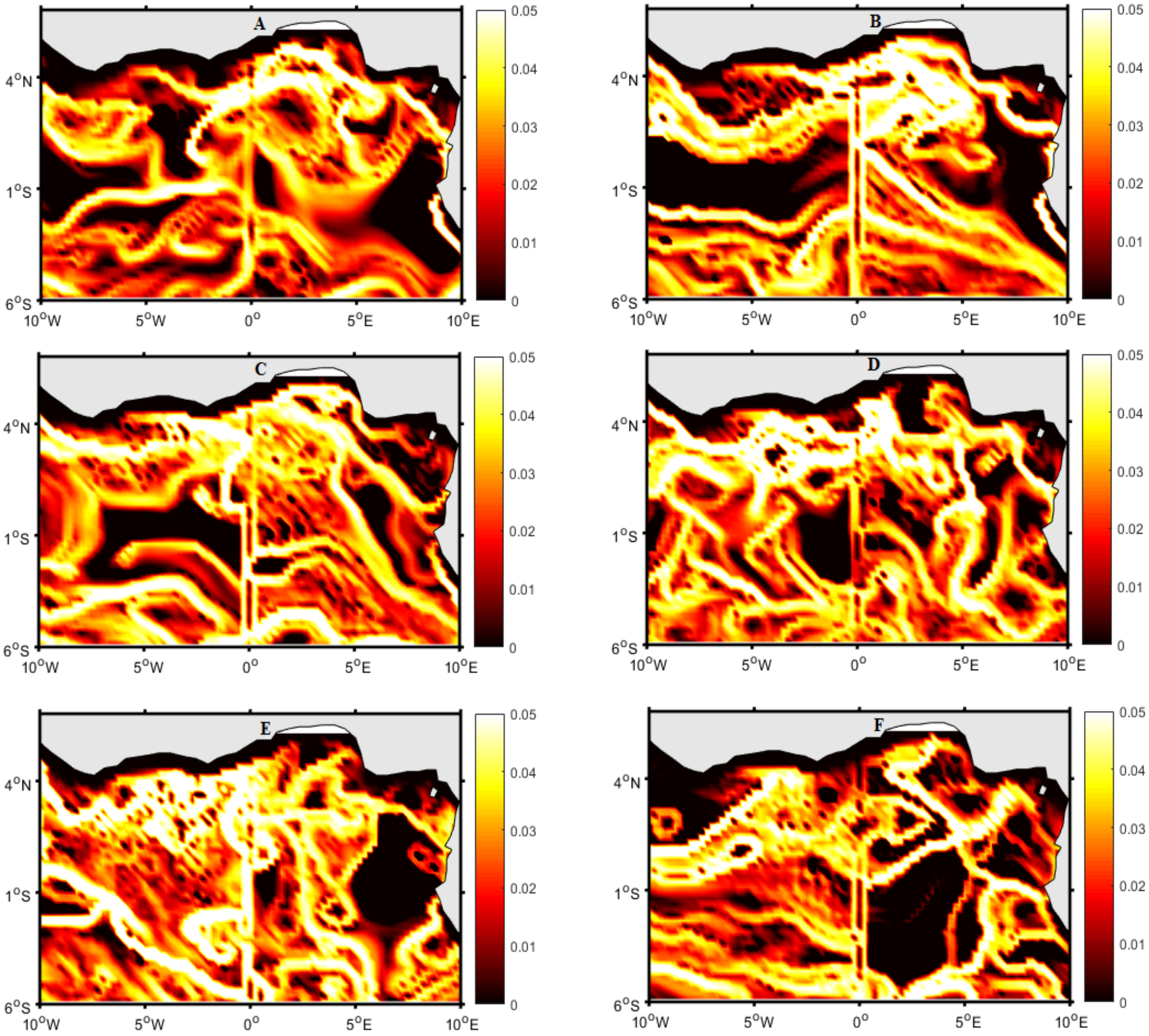

Figure 4.6: The first, fifth, ninth, thirteenth, seventeenth and twenty-first flow maps of the Gulf of Guinea with total integration time of 50 days and time step of 5 days.

From figure 4.6, the LCSs are visualized as time dependent curves in the fluid flow. With the repelling LCSs represented by yellowish and whitish curves and the attracting LCSs are also represented by the reddish curves and black patches in the flow. Also the grey section in the figures represent the coastlines of Cote D'Ivoire, Ghana, Togo, Nigeria and parts of Cameroon. Figures 4.6**A** and 4.6**B** indicate attracting LCSs in many parts of the flow with the highest attracting point for 4.6**C** located between 5°E,1°S and 10°E,1°S . Also for 4.6**B** the highest attracting point are located between 10°W,1°S and 0°E,1°S. Furthermore, repelling curves are formed in most parts of the flow with a concentration of high repelling curves centred at about 0°E,4°N for both figures 4.6**A** and 4.6**B**. Subsequently, figures 4.6**C** and 4.6**D** also indicates less attracting LCSs formed in the Gulf of Guinea and there are a lot of repelling LCSs stretching along 0°E,4°N. Figure 4.6**E** shows the highest case of repelling LCSs stretching from the Coast of Ghana to further parts of the Gulf of Guinea. It is most likely that there will be a rapid divergence of fluid particles at this point in the simulated flow. Finally, in figure 4.6**F**, the number of repelling curves decreases as compared with 4.6**E**. The dominant repelling curve stretching from 10°E,4°N to 10°W,1°S. Also the highest attracting point is located between 0°E,1°S and 5°E,1°S. At these points in the flow, there will be a high rate of mixing of fluid particles. There is a thin straight line at 0°E that divides the FTLE plots into two equal parts. This is as a result of a defect in the satellite data.

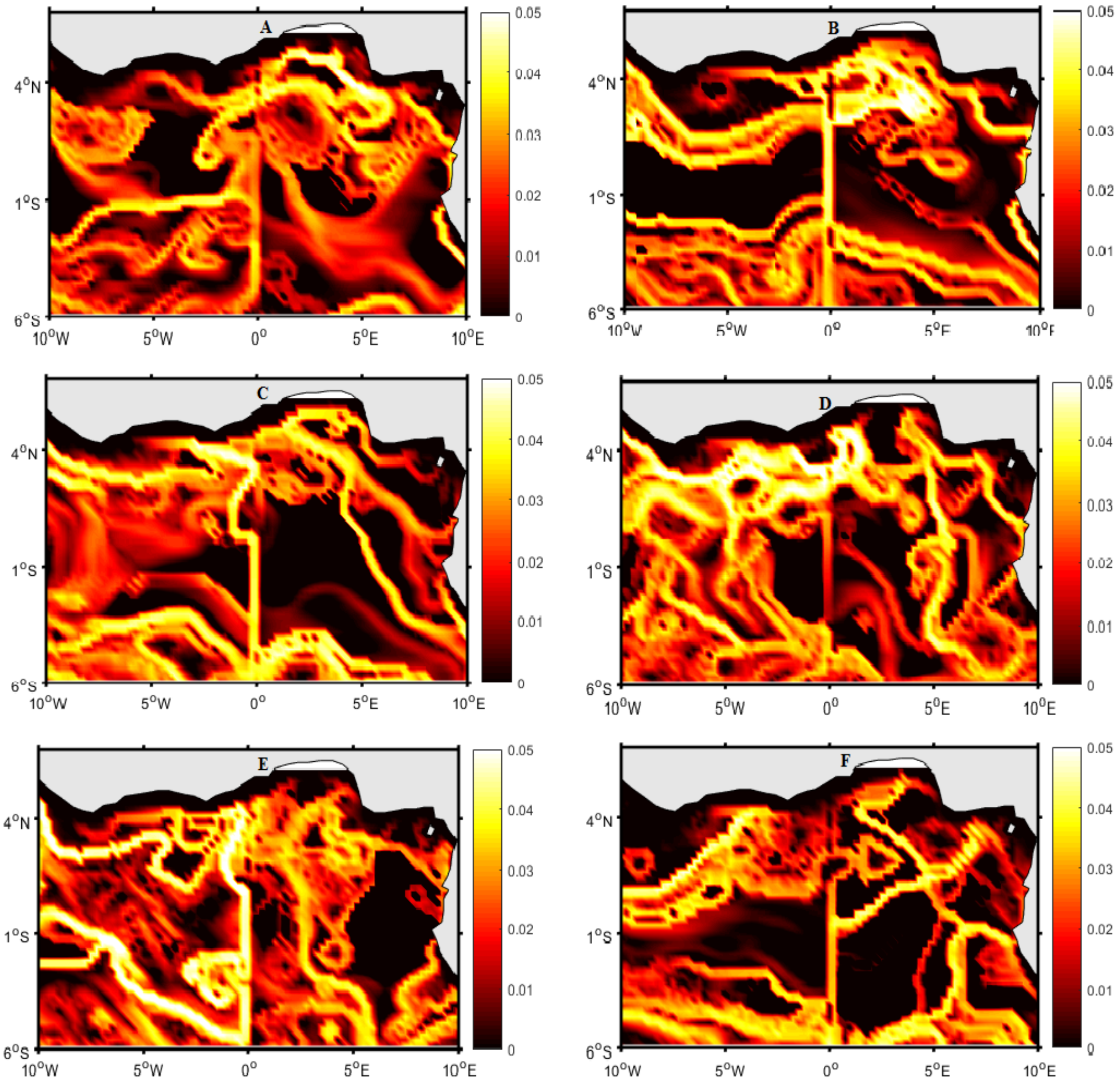

Figure 4.7: The first, fifth, ninth, thirteenth, seventeenth and twenty-first flow maps of the Gulf of Guinea with total integration time of 70 days and time step of 2 days.

In figure 4.7**A** there are more attracting LCSs in the simulated flow with less repelling LCSs. Figure 4.7**B** shows an increase in the repelling curves with high FTLE fields formed at 5°E,3°N. Also in figure 4.7**C**, there is a decline of repelling LCSs curves with the major repelling line stretching from 0°E,6°S. Figure 4.7**D** indicates an increase in the repelling curves as compared with 4.7**C**. Figure 4.7**E** shows a particular repelling LCS that bounds 0°E,4°N and 10°W,1°S. Fluid particles within this region would be confined for sometime due to the repulsion effect of the repelling LCSs. Finally, figure 4.7**F** shows only traces of repelling curves in the flow.

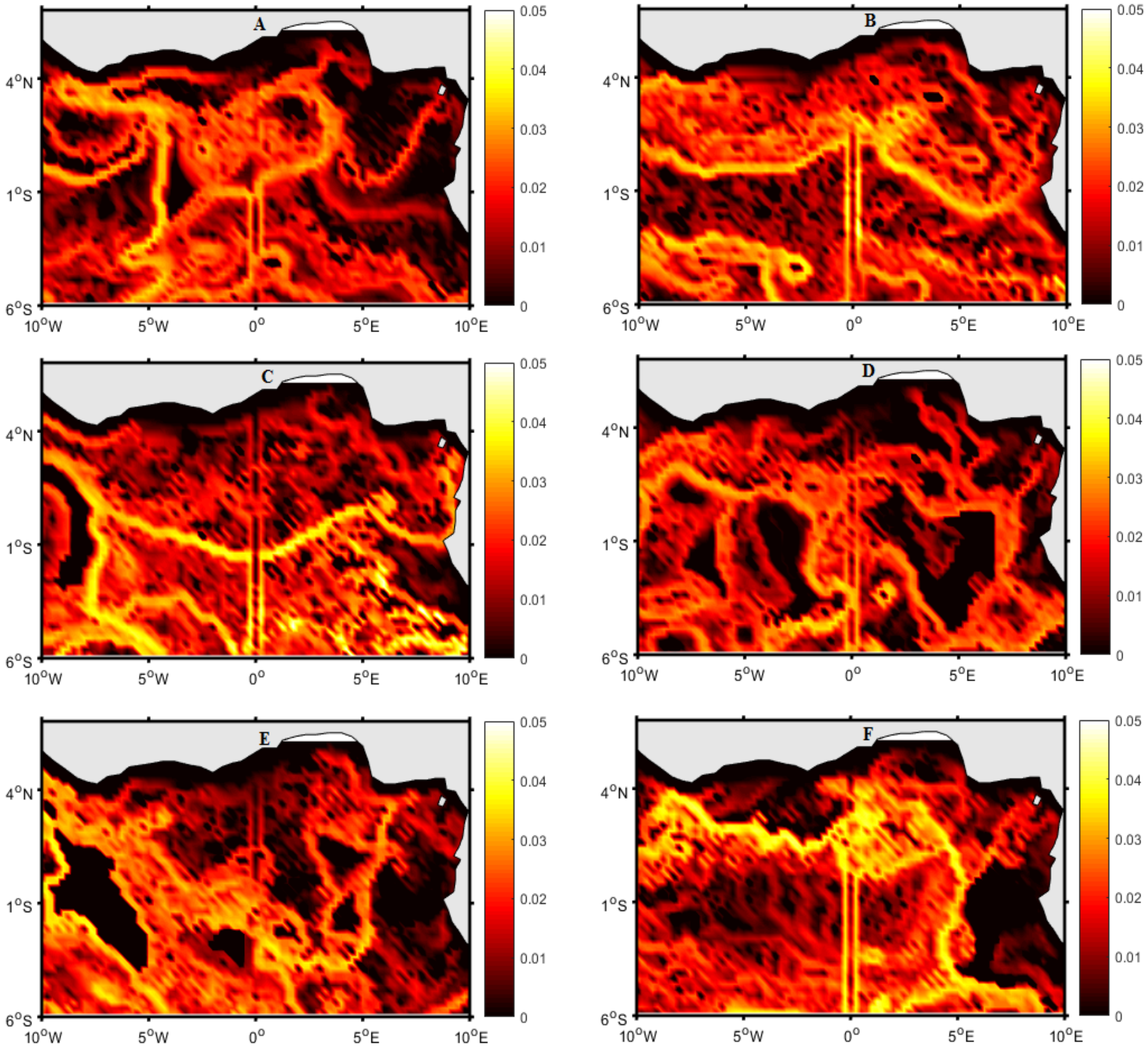

Figure 4.8: The first, fifth, ninth, thirteenth, seventeenth and twenty-first flow maps of the Gulf of Guinea with total integration time of 100 and time step of 10 days.

Figures 4.8**A**, 4.8**B** shows traces of repelling LCSs in the Gulf of Guinea. In figure 4.8**C**, there is one main curve that stretches across the Gulf of Guinea with traces of high FTLE fields in other parts of the flow. Figures 4.8**D** and 4.8**E** show only traces of repelling LCSs scattered within the flow. Figure 4.8**F** has the highest case of repelling LCSs in the simulated flow as compared with all the other figures.

4.4 Discussion of Results

From all the numerical computations on the Gulf of Guinea, it was observed that there was a lot of repelling LCSs in the flow particularly centred along the coastal belt of Ghana at 50 days. The coastal belt of Ghana is our region of interest. When the total integration time was increased to 70 days, there were still regions of high FTLE along the coast of Ghana, however, the concentration of repelling curves was less as compared with the initial integration time. Also when the total integration time was increased from 70 to 100 days, there was a further decline in the number of repelling curves in the flow. Therefore, it was realized that more repelling LCSs are formed for shorter integration times and for longer integration times there are less repelling LCSs in the simulated flow. This may be due to the fact that at longer integration time, the repelling curves have exited the Gulf of Guinea. The main goal of this numerical simulation was to determine the nature of the LCSs located along Ghana's coastline so as to be able to predict what will happen in the event of an oil spill. In the case of an oil spill along the coast of Ghana at $T = 50$, due to the presence of high repelling curves close to the coastline, the oil spill will most likely be pushed onshore. At $T = 70$, it is most likely that the oil spill will be confined to the coast of Ghana because the repelling LCSs would serve as transport barriers by preventing the oil spill from crossing over to a different part of the Gulf of Guinea. At this point, the oil spill can be contained, isolated and cleaned to prevent further harm to aquatic organisms and also humans. Finally, for $T = 100$, due to the decrease in the repelling LCSs and also there being a lot of attracting LCSs, the oil spill would likely be advected along the main repelling LCSs away from the coast of Ghana. However, oil spills have a smoothing effect on water and therefore it can cause a change in the dynamics of the simulated flow. Since this has not been looked at, it can be considered in future works so as to provide a better understanding of the flow dynamics in the event of a spill.

4.5 Implications for Oil spills on the Gulf of Guinea

Crude oil spill is the release of liquid hydrocarbons into the environment from offshore platforms, drilling rigs and wells. Due to it's immiscible property and calming effect on water, it has the propensity to spread for several nautical miles forming an oil slick. There has been an upsurge of crude oil spills since the 1990's and in most third world countries there has not been any proper monitoring system in place to check for these spills. This is because most of the existing models such as the remote sensors are very expensive to use and also due to the complexity of some other models. Oil spills have a hazardous effect on aquatic plants and animals. For the former it cuts off the supply of sunlight and air over the area it covers and with the latter due to it's toxic components it kills organism that are exposed to it.

In Ghana, majority of the populace depend on the marine waters for fishing. Ghana consumes approximately $950,000$ metric tons of fish annually and also import 60 percent of its fish. Most of these products come from the Gulf of Guinea. In light of the fact that Ghana extracts crude oil on a daily basis from the Gulf, it is very alarming that it also obtains other products from the same source. Crude oil has been shown to contain poisonous chemical constituents which can affect most marine organisms when it is ingested or by external exposure. These organisms can either die as a result or they are harvested by fisherfolk who sell them for domestic consumption. Subsequently, consuming these contaminated marine organisms can lead to some short term diseases such as: memory loss, headache, nausea and vomiting and a lot more. Also, it can cause some long term diseases such as: Lung cancer, skin cancer and leukaemia. Therefore, the implications of oil spills on the gulf of Guinea are to be taken seriously.

Due to the fact that there have not been any reported spills or there have been smaller spills which have not been termed significant enough to report. It is therefore important to implement a model which can be used to track crude oil if there should be a spill. The FTLE model can be used to detect trajectories of the particles in a unsteady flow. Using the Cauchy green strain tensor, it computes for the eigenvectors of the system. Based on the backward and forward time integration, the FTLE field is able to expose hyperbolic LCSs in the flow by numerical computations using the velocity fields. Both integration steps are vital in determining repelling structures in the flow. For the backward time integration, it computes the position from which a particle was advected over a time step [20]. Also, forward time integration computes the position to which a particle will be advected during a time step[20]. It is hoped that computations of the FTLE field could be used to forecast the movement of substances in the ocean. The first stage of forecasting is called now-casting and it is defined as the prediction of the current state of a time dependent system using the available information [21]. This helps to detect transport barriers such as vortices and ocean eddies in the flow.

Chapter 5

Conclusion

Transport and mixing are important concepts in tracking of fluid particles in time dependent flows as they have been shown to detect coherent structures that determine the shape of the flow. This project, employed the Finite Time Lyapunov Exponent (FTLE) method to help identify Lagrangian Coherent Structures (LCSs)in an unsteady flow, with a long term plan of tracking oil spills along the coast of Ghana. Chapter 1 introduced the problem of pollution,the motivation of this research and the concepts of LCSs and FTLE. The second chapter reviewed some research papers on LCSs and the FTLE. Chapter 3 starts with a comprehensive study of time-dependent systems. The solutions and phase plots of these systems presented in detail. For instance, the saddle plots of autonomous system and the periodic plots of the simple pendulum. It was realized that they provided a standard for understanding the notion of stable and unstable manifolds which separate dynamically distinct regions. Two definitions of the LCSs were presented. First approach considers it as material line for which a definition was given. In the second approach the LCSs is defined as a second derivative ridge of the FTLE field.

Chapter 4 mainly comprises of the double gyre model and the detection of LCSs in the Gulf of Guinea. The first part looked at the time-independent and time dependent double gyre example. For the former, it was realized that the boundary remained at the same position after the total integration time. This was due to the amplitude of motion being set to zero. Also, for time dependent gyre, the value of amplitude of motion was varied and this causes the boundary to move. The velocity vector plots displayed the trajectories of the gyres rotating in opposite directions. Also the velocity vectors clearly showed the movement of the boundary within the time-dependent gyre. The FTLE plots indicated the highest repelling ridges as red curves and it is likely that fluid particles close to these points will experience a rapid divergence. Secondly in this chapter, the FTLE model was applied on a real satellite data on the ocean velocity fields of the coast of West Africa with our region of interest being the coastline of Ghana. However, for a better analysis to be made, we considered the Gulf of Guinea to enable us investigate the progression of the LCSs in the simulated flow. The surface velocities, the longitude and latitude was extracted for the numerical simulations on the Gulf of Guinea. From the analysis it was realized that more repelling LCSs are formed along the coast of Ghana for a shorter time of integration as compared with a longer time. This finding was important in investigating the occurrence of an oil spill along Ghana's coastline. The main result suggests that it is most likely oil spills will be confined at the coast of Ghana for shorter periods however as time progresses the spill would most likely be advected away from the coastline of Ghana. One of the limitations of this project is that the velocity fields that we obtained did not include active tracer like oil particles.

An extension of this project would involve advecting a tracer (pollutant) in the simulated flow and computing for the velocity fields to determine the advection path of the tracer as time progresses. This would serve as a good grounds to identify other transport barriers such as eddies, vortices and fronts that may be embedded in the flow along the coast of Ghana. As a result, this will then enable us to be able to give an accurate prediction of the advection path of an oil spillage in case it occurs.

References

[1] (Accessed in June 2018). *PRODUCT USER MANUAL FOR Global Ocean Multi Observation Products.* COPERNICUS MARINE ENVIRONMENT MONITORING SERVICE (April,2018) `CMEMS-MOB-PUM-015-001`.

[2] (Accessed 19 July 2018). *A Mapping package for Matlab.* Mmap(May 20th, 2018) `http://www.eos.ubc.ca/~rich/map.html`.

[3] Britannica, E. et al. (2009). *Encyclopædia britannica.* Chicago: Common Law.

[4] Campbell, C. J. and Laherrère, J. H. (1998). *The end of cheap oil.* Scientific American, 278(3):78–83.

[5] Devaney, R. L., Siegel, P. B., Mallinckrodt, A. J., and McKay, S. (1993). *A first course in chaotic dynamical systems: theory and experiment.* Computers in Physics, 7(4):416–417.

[6] D.L.Vokov (April, 2008). *Manual on how to use OceanFTLE1.0 Matlab package.*

[7] Farazmand, M. and Haller, G. (2012). *Computing Lagrangian coherent structures from their variational theory.* Chaos: An Interdisciplinary Journal of Nonlinear Science, 22(1):013128.

[8] Hadjighasem, A. (2016). *Extraction of Dynamical Coherent Structures from Time-Varying Data Sets.* PhD thesis, ETH Zurich.

[9] Haller, G. (2011). *A variational theory of hyperbolic Lagrangian coherent structures.* Physica D: Nonlinear Phenomena, 240(7):574–598.

[10] Haller, G. (2015). *Lagrangian coherent structures.* Annual Review of Fluid Mechanics, 47:137–162.

[11] Haller, G. and Yuan, G. (2000). *Lagrangian coherent structures and mixing in two-dimensional turbulence.* Physica D: Nonlinear Phenomena, 147(3-4):352–370.

[12] Huhn, F., Kameke, A., Pérez-Muñuzuri, V., Olascoaga, M., and Beron-Vera, F. (2012). *The impact of advective transport by the South Indian Ocean Countercurrent on the Madagascar plankton bloom.* Geophysical Research Letters, 39(6).

[13] La Salle, J., Lefschetz, S., and Alverson, R. (1962). *Stability by Liapunov's direct method with applications.* Physics Today, 15:59.

[14] Michel, A., Wang, K., and Hu, B. (2001). *Qualitative theory of dynamical systems*, volume 239. CRC Press.

[15] Nave Jr, G. K. and Ross, S. D. (2017). *Trajectory-free calculation of attracting and repelling manifolds.* arXiv preprint arXiv:1705.07949.

[16] Nencioli, F., d'Ovidio, F., Doglioli, A., and Petrenko, A. (2011). *Surface coastal circulation patterns by in-situ detection of Lagrangian coherent structures.* Geophysical Research Letters, 38(17).

[17] Olascoaga, M. J. and Haller, G. (2012). *Forecasting sudden changes in environmental pollution patterns.* Proceedings of the National Academy of Sciences.

[18] O'neill, B. (2006). *Elementary differential geometry.* Academic press.

[19] Onu, K., Huhn, F., and Haller, G. (2015). *LCS Tool: A computational platform for Lagrangian coherent structures.* Journal of Computational Science, 7:26–36.

[20] Ourmieres, Y., Mansui, J., Molcard, A., Galgani, F., and Poitou, I. (2018). *The boundary current role on the transport and stranding of floating marine litter: The French Riviera case.* Continental Shelf Research, 155:11–20.

[21] Peacock, T. and Dabiri, J. (2010). *Introduction to focus issue: Lagrangian coherent structures.*

[22] Peacock, T. and Haller, G. (2013). *Lagrangian coherent structures: The hidden skeleton of fluid flows.* Physics today, 66(2):41–47.

[23] Peng, J. and Peterson, R. (2012). *Attracting structures in volcanic ash transport.* Atmospheric environment, 48:230–239.

[24] Shadden, S. C., Lekien, F., and Marsden, J. E. (2005). *Definition and properties of Lagrangian coherent structures from finite-time Lyapunov exponents in two-dimensional aperiodic flows.* Physica D: Nonlinear Phenomena, 212(3-4):271–304.

[25] Shadden, S. C., Lekien, F., Paduan, J. D., Chavez, F. P., and Marsden, J. E. (2009). *The correlation between surface drifters and coherent structures based on high-frequency radar data in Monterey Bay.* Deep Sea Research Part II: Topical Studies in Oceanography, 56(3-5):161–172.

[26] Tallapragada, P., Ross, S. D., and Schmale III, D. (2011). *Lagrangian coherent structures are associated with fluctuations in airborne microbial populations.* Chaos: An Interdisciplinary Journal of Nonlinear Science, 21(3):033122.

[27] Voth, G. A., Haller, G., and Gollub, J. P. (2002). *Experimental measurements of stretching fields in fluid mixing.* Physical review letters, 88(25):254501.

[28] White, R. (2008). *Toxic cities: Globalizing the problem of waste.* Social Justice, 35(3 (113):107–119.